PAPER

Check for updates

Hydrodeoxygenation and hydrodenitrogenation of *n*-hexadecanamide over Pt catalysts: effect of the support†

Emma Verkama, [iD] *[a] Sylvia Albersberger,[b] Aitor Arandia, [iD] ‡[a] Kristoffer Meinander,[c] Marja Tiitta, [iD] §[b] Reetta Karinen [iD] [a] and Riikka L. Puurunen [iD] [a]

Efficient catalysts for simultaneous hydrodeoxygenation (HDO) and hydrodenitrogenation (HDN) are needed for the production of renewable fuels. In this study, Pt catalysts supported on SiO_2, γ-Al_2O_3, SiO_2–Al_2O_3, ZrO_2, CeO_2–ZrO_2, Nb_2O_5, and TiO_2 were studied for the hydrotreatment of *n*-hexadecanamide (C16 amide) to *n*-paraffins at 300 °C and 80 bar H_2. The catalysts favored HDO over HDN, and the initial differences in the nitrogen removal level were smaller than the differences in the oxygen removal level. The Lewis acid properties of the support influenced the initial C16 amide conversion route and HDO activity, which was reflected in the reaction network and condensation reaction selectivity of the catalysts. Pt/Nb_2O_5 and Pt/TiO_2, with intermediate strength Lewis acid sites, initially favored the HDO of C16 amide to nitrogen-containing compounds. In contrast, the other catalysts converted C16 amide to oxygen- and nitrogen-containing compounds with similar selectivity. The HDO of the oxygen-containing compounds proceeded more efficiently on the Pt catalysts supported on oxides with weak Lewis acid sites (Pt/ZrO_2, Pt/CeO_2–ZrO_2) than on the irreducible oxides with strong or no Lewis acid sites (Pt/γ-Al_2O_3, Pt/SiO_2–Al_2O_3, Pt/SiO_2). As the presence of oxygen-containing compounds suppressed HDN activity, the catalysts with the highest HDO activity eventually gave the highest paraffin yield, regardless of which oxygen removal pathway was favored.

1. Introduction

Renewable fuels with a high energy density are needed to mitigate the CO_2 emissions from the heavy-duty transport sector and aviation industry. Major research efforts have been devoted to the hydrodeoxygenation (HDO) of renewable feedstocks to fuels due to their significant oxygen content.[1–8] Hydrodenitrogenation (HDN) has received less attention, even though nitrogen-containing compounds are present in renewable feedstocks, such as animal fats and algal biocrudes.[9,10] Since nitrogen-containing compounds can poison catalysts in downstream processing units and negatively impact fuel stability, the nitrogen content of

feedstocks needs to be reduced along with the oxygen content.[11]

A high HDO activity and the ability to catalyze C–N bond hydrogenolysis make supported noble metal catalysts an alternative to transition metal sulfide catalysts for the hydrotreatment of sulfur-free feedstocks.[7,8,12–15] In our previous study on the co-hydrotreatment of fatty acids and alkyl amines on Pt/ZrO_2, we found that HDN was inhibited by the HDO of oxygen-containing intermediates and the formation of secondary amines and amides through condensation reactions.[16] An information gap remains for the application of noble metal catalysts in the simultaneous HDO and HDN of molecules that contain both oxygen and nitrogen and on the effect of the catalyst composition on the relative HDO and HDN activity. These topics are addressed in this study.

Primary amides are present in feedstocks that are used for the production of renewable fuels, which makes them relevant model compounds for studying simultaneous HDN and HDO.[10,17] Nevertheless, the HDN and HDO of primary amides to different paraffins remain sparsely studied, whereas the hydrogenation of secondary and tertiary amides to amines and alcohols on supported noble metal catalysts has been reported previously.[18–28] Liu *et al.*[26] evaluated Co/

[a] *Department of Chemical and Metallurgical Engineering, School of Chemical Engineering, Aalto University, P.O. Box 16100, 00076 Aalto, Finland.*
E-mail: emma.verkama@aalto.fi
[b] *Neste Corporation, P.O. Box 310, 06101 Porvoo, Finland*
[c] *Department of Bioproducts and Biosystems, School of Chemical Engineering, Aalto University, P.O. Box 16300, 00076 Aalto, Finland*
† Electronic supplementary information (ESI) available. See DOI: https://doi.org/10.1039/d3cy01480k
‡ VTT Technical Research Centre of Finland Ltd. P.O. Box 1000, FI-02044 Espoo, Finland.
§ 06650 Hamari, Finland.

This journal is © The Royal Society of Chemistry 2024

Catal. Sci. Technol., 2024, **14**, 431–448 | 431

SiO$_2$, Co/γ-Al$_2$O$_3$ and Co/H-ZSM-22 in the co-hydrotreatment of palmitic acid and *n*-hexadecanamide. The reaction products comprised *n*-paraffins (C14–C16), iso-paraffins (C15–C16) and 1-hexadecanol, and the hydrotreatment of *n*-hexadecanamide was proposed to proceed through *n*-hexadecanal.[26] The catalyst with the highest overall acidity, Co/H-ZSM-22, showed the highest activity and favored the formation of normal and branched C16 paraffins through C–O bond hydrogenolysis, while the less acidic Co/SiO$_2$ and Co/γ-Al$_2$O$_3$ catalysts exhibited a lower activity level and favored decarbonylation and decarboxylation routes.[26] Shimizu *et al.*[18] likewise found that the support strongly influenced the activity of Pt-based catalysts for the selective HDO of *n*-acetyl piperidine to the corresponding amine.[18] Pt/ Nb$_2$O$_5$ emerged as a highly active catalyst for the reaction, which was attributed to Lewis acid–base interactions between the Lewis acid sites of the partially reduced Nb$_2$O$_5$ support and the carbonyl group of the amide.[18]

The acidity and reducibility of the catalyst support are known to affect the activity and selectivity of noble metal catalysts in the HDO of oxygen-containing compounds.[14,29–31] Lewis acid sites bond to and activate carbonyl and hydroxyl groups, whereas Brønsted acid sites confer dehydration and isomerization activity.[14,31–33] The enhancing effect of reducible supports on HDO activity has been attributed to the catalytic activity of oxophilic Lewis acid sites for materials such as ZrO$_2$ and CeO$_2$–ZrO$_2$, and strong metal–support interactions for materials such as Nb$_2$O$_5$ and TiO$_2$.[29,32,34–37] Based on HDO studies on supported noble metal catalysts and the findings of Liu *et al.*[26] and Shimizu *et al.*,[18] the acidity and reducibility of the catalyst support can therefore be expected to influence the activity and selectivity of noble metal catalysts in the HDN and HDO of primary amides.

In this study, Pt catalysts supported on SiO$_2$, γ-Al$_2$O$_3$, two SiO$_2$–Al$_2$O$_3$ materials, ZrO$_2$, CeO$_2$–ZrO$_2$, Nb$_2$O$_5$, and TiO$_2$ were studied for the hydrotreatment of *n*-hexadecanamide (C16 amide, C$_{16}$H$_{33}$NO). C16 amide was chosen as a model compound due to the presence of primary amides in feedstock relevant to the production of renewable fuels, whereas the supports were chosen due to their diverse acid and redox properties.[10,17] The purpose of this study was to describe the effect of the support on the catalytic activity and selectivity in the HDO and HDN of C16 amide and to discuss the active sites for the reactions based on the catalyst characterization and activity test data. To the best of our knowledge, the effect of the support on the activity and selectivity of Pt catalysts for the simultaneous HDO and HDN of molecules that contain oxygen and nitrogen has not been reported before.

2. Experimental

2.1 Materials

For catalyst preparation, platinum(IV) nitrate solution (Alfa Aesar, 15 wt% Pt) was used as the platinum precursor. The following materials were used as catalyst supports: TiO$_2$ (44429, Alfa Aesar), ZrO$_2$ (SZ 31164, Saint-Gobain Norpro), SiO$_2$ (silica gel, Davisil Grade 646, Sigma-Aldrich), γ-Al$_2$O$_3$ (calcined from Pural NW Boehmite, Sasol), 5 wt% SiO$_2$/Al$_2$O$_3$ (5SiO$_2$–95Al$_2$O$_3$, Siralox5, Sasol), 30 wt% SiO$_2$/Al$_2$O$_3$ (30SiO$_2$– 70Al$_2$O$_3$, Siralox30, Sasol), 25 wt% CeO$_2$/ZrO$_2$ (CeO$_2$–ZrO$_2$, XZO 1290, MEL Chemicals), and Nb$_2$O$_5$ (calcined from niobium oxide hydrate, Companhia Brasileira de Metalurgia e Mineração).

The following chemicals were used without further purification for the reactor experiments and calibrations: *n*-hexadecanamide (>95%, Tokyo Chemical Industry), decalin (decahydronaphthalene, anhydrous, mixture of cis and trans, >99%, Sigma Aldrich), *n*-pentadecane (>99%, Aldrich), *n*-hexadecane (>99%, Sigma Aldrich), *n*-hexadecanal (>97%, Tokyo Chemical Industry), 1-hexadecanol (96%, Acros Organics), palmitic acid (>98%, Riedel de Haën), 1-hexadecylamine (>95%, Tokyo Chemical Industry), *n*-pentadecanonitrile (>95%, Tokyo Chemical Industry), *n*-heptadecanonitrile (>95%, Tokyo Chemical Industry), palmityl palmitate (>99%, Sigma Aldrich), *n*-dodecane (>99%, Merck), and 2-propanol (>99%, Riedel de Haën). The pyridine used for acid site characterization was obtained from Sigma Aldrich (anhydrous, 99.8%).

The gases used for the reactor experiments, catalyst characterization and product analysis (H$_2$, He, N$_2$ O$_2$, Ar, and synthetic air) were all of 99.999% purity and were acquired from AGA and Woikoski. The helium and synthetic air used in the pyridine Fourier transform infrared spectroscopy (FTIR) measurements were obtained from Linde. The 5 vol% CO$_2$/He (99.999%/99.999%) gas mixture was obtained from Woikoski, whereas the 2 vol% H$_2$/Ar (99.999%/99.999%) gas mixture was purchased from AGA.

2.2 Catalyst preparation

The catalysts were prepared using a vacuum impregnation method with a small excess of liquid. The supports were crushed and sieved to a particle size of 0.25–0.42 mm and calcined in ambient air in a static muffle furnace for 10 h prior to impregnation (250 °C for 5SiO$_2$–95Al$_2$O$_3$, 450 °C for TiO$_2$ and CeO$_2$–ZrO$_2$, 500 °C for Nb$_2$O$_5$, and 600 °C for γ-Al$_2$O$_3$, SiO$_2$, 30SiO$_2$–70Al$_2$O$_3$, and ZrO$_2$). The impregnation and calcination were carried out as described previously.[16]

2.3 Catalyst characterization

2.3.1 N$_2$-physisorption. A Surfer instrument from Thermo Scientific was used to carry out isothermal N$_2$-physisorption measurements at −196 °C for 200 mg samples of the calcined catalysts. In order to remove moisture and adsorbed compounds, the samples were first degassed in a vacuum at 350 °C for 180 min before the measurements, using a 5 °C min^{-1} heat ramp. Liquid nitrogen was used as a coolant, and a dead volume calibration was carried out with helium after every measurement. The specific surface area S_{BET} (m^2 g^{-1}) was calculated from the adsorption isotherm using the Brunauer–Emmett–Teller (BET) method.[38] The pore volume

432 | *Catal. Sci. Technol.*, 2024, **14**, 431–448

This journal is © The Royal Society of Chemistry 2024

V_{pore} (cm^3 g^{-1}), pore size distribution, and mean pore diameter $d_{pore,mean}$ (nm) were calculated from the desorption branch using the Barrett–Joyner–Halenda (BJH) method.[39]

2.3.2 Scanning transmission electron microscopy. Scanning transmission electron microscopy (STEM) images were taken of the calcined catalysts using a JEOL JEM-2200FS aberration-corrected high-resolution electron microscope operating at a 200 kV acceleration voltage. For the measurements, the samples were drop-cast with acetone onto copper grids and coated with an ultrathin carbon film. The diameter of 100–200 platinum particles was measured for each catalyst, using the ImageJ software, to estimate the platinum particle size distribution and the mean platinum particle size d_{Pt} (nm).

2.3.3 X-ray fluorescence. A semi-quantitative estimation of the platinum loading (wt%) was obtained using X-ray fluorescence (XRF) with a wavelength-dispersive PANalytical Axios mAx equipment. The measurements were conducted in helium for approximately 200 mg samples of ground, calcined catalyst. The samples were measured as loose powders in Chemplex 1330-SE sample cups covered with a 3.6 μm Mylar film.

2.3.4 X-ray diffraction. X-ray diffraction (XRD) was carried out to identify the crystallographic phase of the catalysts. A PANalytical X'Pert PRO MPD Alpha-1 X-ray diffractometer, with Cu Kα1 radiation (45 kV, 40 mA), was used for the measurements. The 2θ scanning range was from 5° to 100°, with a step size of 0.026°. The analysis was conducted for ground samples of the calcined catalysts. The HighScore software was used for phase identification (ICDD PDF-4+ 2023 database).

2.3.5 X-ray photoelectron spectroscopy. X-ray photoelectron spectroscopy (XPS) measurements were performed for the catalysts using a Kratos AXIS Ultra DLD X-ray photoelectron spectrometer with a monochromated Al$_{K\alpha}$ X-ray source (1486.7 eV) run at 100 W. A pass energy of 80 eV and a step size of 1.0 eV were used for the survey spectra, while a pass energy of 20 eV and a step size of 0.1 eV were used for the high-resolution spectra. Photoelectrons were collected at a 90° take-off angle under ultra-high vacuum conditions, with a base pressure typically below 1 × 10^{-9} Torr. The diameter of the beam spot from the X-ray was 1 mm, and the area of analysis for these measurements was 300 μm × 700 μm. Both survey and high-resolution spectra were collected from three different spots on each sample surface in order to check for homogeneity and surface charge effects. All spectra were charge-corrected relative to the position of C–C bonds at 284.8 eV. Data analysis was carried out using the CasaXPS software. The catalyst samples were reduced *ex situ* at 350 °C in 2 vol% H$_2$/Ar for 60 min before the measurements.

The Pt 4f spectra were fit using five doublets for metallic Pt(0), Pt(I), Pt(II), Pt(IV), and a mixed state located between Pt(I) and Pt(II). The binding energies for the Pt 4f$_{7/2}$ of these components were located at approximately 71.0 eV, 72.2 eV, 73.5 eV, 74.5 eV, and 72.7 eV, respectively. For the Al$_2$O$_3$-containing catalysts, an additional peak at 74.9 eV was used for Al 2p due to the overlap of Pt 4f and Al 2p. The full width at half maximum (FWHM) for all Pt peaks was approximately 1.4 eV, with an energy separation between the doublets of 3.35 eV, while the FWHM for the Al component was 2.4 eV. For the Pt/SiO$_2$, Pt/Al$_2$O$_3$, Pt/5SiO$_2$–95Al$_2$O$_3$, and Pt/30SiO$_2$–70Al$_2$O$_3$ catalysts, the O 1s spectra were deconvoluted using two Gaussian components of equal FWHM. One component was used for lattice oxygen and one for surface hydroxyls, at binding energies approximately 1.0–1.5 eV higher than the lattice oxygen. For Pt/ZrO$_2$, Pt/CeO$_2$–ZrO$_2$, Pt/Nb$_2$O$_5$, and Pt/TiO$_2$, an additional minor Gaussian component at approximately 533.3 eV, possibly related to oxygen bound to organic contaminants, was used. The C 1s spectra of all catalysts were fitted using four Gaussian components according to standard tabulated chemical shifts, with peak positions at 284.8 eV (C–C), 286.5 eV (C–O), 287.8 eV (C=O), and 288.9 eV (O–C=O). The relative intensities for the carbon components corresponded to adventitious carbon.

The Si 2p spectra of the Pt/SiO$_2$, Pt/5SiO$_2$–95Al$_2$O$_3$, and Pt/30SiO$_2$–70Al$_2$O$_3$ catalysts were fitted using a single Gaussian at approximately 103.0 eV, corresponding to silicon oxide. The Ti 2p spectra of Pt/TiO$_2$ and the Nb 3d spectra of Pt/Nb$_2$O$_5$ were fitted using single component doublets, with the Ti 2p$_{3/2}$ at an energy of 458.7 eV and the Nb 3d$_{5/2}$ at an energy of 207.3 eV. The Zr 3d spectra of the Pt/ZrO$_2$ and Pt/CeO$_2$–ZrO$_2$ catalysts were fitted using two doublets, with the 3d$_{5/2}$ peaks located at 182.1 eV and 183.4 eV. For Pt/CeO$_2$–ZrO$_2$, a fitting scheme similar to that of Bêche *et al.*[40] was adopted to differentiate between Ce(III) and Ce(IV) oxides, using a total of three doublets for the Ce(IV) oxide and two doublets for the Ce(III) oxide.

2.3.6 Temperature-programmed reduction. Qualitative hydrogen temperature-programmed reduction (H$_2$-TPR) measurements were carried out using AMI-200R flow through equipment from Altamira Instruments, which was connected to an OmniStar GSD320 mass spectrometer (MS) from Pfeiffer Vacuum. The catalyst samples (70–120 mg, targeting a constant bed height) were dried by heating from room temperature to 200 °C in He flow with a heating rate of 10 °C min^{-1}, which was followed by a 120 min hold. The samples were then cooled to 30 °C under a He flow. At 30 °C, the samples were flushed in Ar for 30 min. Next, a flow of 2 vol% H$_2$/Ar was introduced to the reactor, and the temperature was increased from 30 °C to 600 °C at a heating rate of 5 °C min^{-1}. The total flow rate was maintained at 50 ml min^{-1} (STP) throughout the measurement. A stepwise linear baseline correction was carried out to compensate for the drift in the MS signals. The data between 30 °C and 60 °C was disregarded in the data treatment and visualization, due to signal fluctuations attributed to the stabilization of the flow rates. Mass-to-charge ratios (m/z) of 2 (H$_2$), 4 (He), 18 (H$_2$O), 28 (N$_2$/CO), 32 (O$_2$), and 40 (Ar) were monitored using the MS.

2.3.7 Temperature-programmed desorption of CO$_2$. Carbon dioxide temperature-programmed desorption (CO$_2$-

TPD) measurements were conducted for the catalysts to quantify their overall basicity. The measurements were conducted using the AMI-200R equipment connected to the OmniStar GSD320 MS for 70–120 mg catalyst samples (targeting a constant bed height). The samples were first dried in He for 2 h at 180 °C, using a heating rate of 10 °C min^{-1}, after which the samples were heated to 350 °C in 2 vol% H$_2$/Ar using a heating rate of 10 °C min^{-1}, and reduced for 2 h. After reduction, the samples were cooled in He to 50 °C, and the temperature was held for a further 30 min. Next, a 0.52 vol% CO$_2$/He flow was directed to the sample at 50 °C and maintained for 30 min, after which the sample was flushed in He for 60 min. Then, the samples were heated to 600 °C in He with a heating rate of 10 °C min^{-1} and kept at 600 °C for 30 min before cooling. A 50 ml min^{-1} (STP) flow was maintained throughout the entire experiment. The desorbed CO$_2$ was quantified by carrying out a one-step calibration for m/z 44. Additionally, m/z 4 (He), 18 (H$_2$O), 28 (N$_2$/CO), and 32 (O$_2$) were monitored using the MS.

2.3.8 Acid site characterization. Acid site characterization was performed using FTIR, with pyridine as the probe molecule. A Thermo Scientific Nicolet iS10 spectrometer, equipped with an *in situ* transmission FTIR cell from Harrick Scientific Products Inc (customized from the HTC-3 model), a liquid-N$_2$ cooled mercury–cadmium–telluride (MCT) detector, and a HeNe laser, was used for the measurements. The spectral range was 4000–650 cm^{-1}, and a spectral resolution of 0.24 cm^{-1} was used.

The catalyst samples (15–30 mg) were pressed into self-supported pellets, 1.1 cm in diameter, with a hydraulic press. The samples were heated in a vacuum to 90 °C with a 5 °C min^{-1} heating rate and maintained for 30 min. Next, the temperature was increased to 450 °C with a 20 °C min^{-1} heating rate and maintained for 60 min. The temperature was then lowered to 170 °C and held for 10 min, after which the spectra of the clean samples were recorded. Next, the samples were saturated with pyridine for 10 min using an atmospheric saturator, followed by evacuation and a 15 min hold. After that, the spectra used to quantify the acidity were recorded.

The Omnic 9.11 software was used to subtract the background and the spectra of the clean samples from the spectra of the pyridine-saturated samples to carry out a stepwise linear baseline correction. Peak integration and deconvolution were carried out using Omnic 9.11 and OriginPro, and the concentration of Lewis and Brønsted acid sites were estimated from the corresponding peak areas and sample weight using the relationships presented by Emeis.[41]

2.4 Catalytic activity tests

The catalytic activity tests were carried out in a 100 ml high-pressure Hastelloy batch reactor by Parr Instrument Company, which was equipped with a heated feed vessel. The catalyst (20 mg) was dried *in situ* at 180 °C under 10 bar of N$_2$ for 60 min and then reduced at 350 °C under 20 bar of H$_2$

for 60 min. The drying and reduction conditions were adopted from the work by Mäkelä and González Escobedo *et al.*,[30] while the experimental conditions were chosen based on preliminary experiments.

The feed mixture was prepared by dissolving 56.5 mg of *n*-hexadecanamide into 31 ml of decalin under heating (~100 °C), targeting an initial nitrogen concentration of 100 ppm. A 1 ml zero-sample was then taken from the feed mixture, and the feed mixture was transferred to the feed vessel attached to the reactor.

The feed mixture was released from the feed vessel to the reactor, which was pre-heated to 300 °C. The reactor was pressurized to 80 bar H$_2$, and stirring at 600 rpm was initiated, which marked the onset of the reaction time. Once the chosen reaction time of 15–300 min had elapsed, the heating and stirring were stopped, and the reactor was quenched with ice. A reaction time of 60 min was used as a reference for the activity and selectivity comparison of the catalysts and supports. The reactions were studied with respect to batch residence time τ (g$_{cat}$ h g$_{amide}^{-1}$), as defined in eqn (1), to take variations in the initial amounts of catalyst and reactant into account.

$$\tau = \frac{m_{cat}t}{m_A}, \tag{1}$$

Here, m_{cat} is the mass of the catalyst (g), t is the reaction time (h), and m_A is the mass of the reactant at the start of the reaction (g).

The absence of external diffusion limitations was confirmed by conducting experiments while stirring at 200 and 1000 rpm. The repeatability of the experiments was evaluated using three 60 min repetition experiments with the Pt/ZrO$_2$ catalyst, and a 60 min experiment was conducted with a repetition batch of the Pt/ZrO$_2$ catalyst to ensure the repeatability of the catalyst preparation. The 180 min experiment with the Pt/ZrO$_2$ catalyst was also repeated. Fig. S1 of the ESI† displays the product distribution of the control experiments.

2.5 Product analysis

The *n*-hexadecanamide model compound and some of the reaction products are sparsely soluble in decalin and other nonpolar hydrocarbon solvents at room temperature. In order to dissolve the model compound and reaction products, 10–20 vol% of a second solvent (2-propanol) was added to the samples prior to analysis. An internal standard (*n*-dodecane) was also introduced to the samples.

2.5.1 Identification of liquid products. Identification of the products was performed using gas chromatography-mass spectrometry (GC-MS). The GC-MS analysis was carried out using a Shimadzu QP2010SE gas chromatograph mass spectrometer with EI ionization and an Optic 4 injector. The equipment was equipped with an Agilent J&W HP5-MS column (30 m × 0.25 mm × 0.25 μm). The NIST2017 library was used for identification.

434 | *Catal. Sci. Technol.*, 2024, **14**, 431–448

This journal is © The Royal Society of Chemistry 2024

2.5.2 Quantification of liquid products. The liquid reaction products were quantified using an Agilent 7890 gas chromatograph (GC) equipped with an Agilent J&W HP5-MS column (30 m × 0.25 mm × 0.25 μm) or an Agilent J&W HP1-MS column (60 m × 0.25 mm × 0.25 μm), with the outlet split between a flame ionization detector (FID) and a nitrogen phosphorus detector (NPD).

The inlet of the GC was at 325 °C, as was the temperature of both the FID and the NPD. An injection volume of 2 μl and a split ratio 5 : 1 was used. The analysis program used for the HP5 column started with a 3 min hold at 40 °C, from which the temperature was increased to 100 °C at a rate of 20 °C min^{-1} and then held for 3 min. The temperature was increased to 150 °C at a rate of 5 °C min^{-1}, and from there to 325 °C at a rate of 10 °C min^{-1}, where a final 12 min hold took place. For the HP1 column, the analysis program started with a 3 min hold at 80 °C, from which the temperature was increased to 100 °C at a rate of 20 °C min^{-1} and then held for 3 min. The temperature was increased to 160 °C at a rate of 10 °C min^{-1} and from there to 325 °C at a rate of 20 °C min^{-1}, where a final 20 min hold took place.

Weight-based FID response factors, relative to the internal standard n-dodecane, were determined experimentally for n-pentadecane, n-hexadecane, 1-hexadecylamine, 1-hexadecanol, palmitic acid, n-hexadecanamide, n-pentadecanonitrile and n-heptadecanonitrile. The response factors for n-pentadecanonitrile and n-heptadecanonitrile were averaged to obtain an estimate for the response factor of n-hexadecanonitrile. The response factors for n-hexadecyl hexadecylamine, n-hexadecyl hexadecanamide, dipentadecyl ketone and palmityl palmitate were estimated based on their combustion enthalpy, using the procedure by de Saint Laumer et al.[42]

The reactant conversion X_A (%) was calculated using eqn (2),

$$X_A = \frac{n_{A,0} - n_A}{n_{A,0}} \cdot 100\%, \quad (2)$$

where $n_{A,0}$ is the initial amount of reactant (mol), and n_A is the amount of unreacted reactant in the product sample (mol).

The yield for each product Y_P (%) was calculated using eqn (3),

$$Y_P = \frac{\mu_P n_P}{n_{A,0}} \cdot 100\%, \quad (3)$$

where μ_P is a stoichiometric factor (two for the C32 compounds and one for the other products), and n_P is the amount of product P in the product sample (mol).

The oxygen removal (O-removal, %) was estimated from the product distribution, using eqn (4),

$$\text{O-removal} = \frac{c_{O,products}}{c_{O,feed}} \cdot 100\%, \quad (4)$$

where $c_{O,products}$ is the oxygen content calculated from the composition of the product sample (ppm), and $c_{O,feed}$ is the oxygen content calculated from the composition of the feed mixture (ppm). In this work, ppm is defined as mg L^{-1}.

The molar carbon balance closure B_C (%) was calculated using eqn (5),

$$B_C = \frac{n_{C,products}}{n_{C,feed}} \cdot 100\%, \quad (5)$$

where $n_{C,products}$ is the amount of carbon quantified from the product mixture (mol), and $n_{C,feed}$ is the amount of carbon quantified from the feed mixture (mol).

The molar carbon balance closure was generally above 90% for the catalytic experiments. The molar carbon balance closures for tests of the bare ZrO_2, CeO_2–ZrO_2, and TiO_2 supports were lower (~85%), indicating that some products remained undetected or adsorbed on the surface of the supports.

2.5.3 Total nitrogen content analysis. The total nitrogen content of the feed and liquid reaction products was analyzed using an AntekPAC ElemeNtS analyzer, calibrated for nitrogen contents between 0 and 1000 ppm with standard calibration solutions (AC Analytical Controls BV). The nitrogen removal (N-removal, %) was calculated using eqn (6),

$$\text{N-removal} = \frac{c_{N,products}}{c_{N,feed}} \cdot 100\%, \quad (6)$$

where $c_{N,products}$ is the nitrogen content of the product sample (ppm), and $c_{N,feed}$ is the nitrogen content of the feed mixture (ppm).

Table 1 Properties of the calcined Pt catalysts obtained from N$_2$-physisorption measurements and derived from STEM images

Catalyst	N$_2$-physisorption			STEM	
	S_{BET} (m^2 g^{-1})	$d_{pore,mean}$ (nm)	V_{pore} (cm^3 g^{-1})	d_{Pt} (nm)	Standard deviation, d_{Pt} (nm)
Pt/SiO$_2$	289	15	0.98	1.8	0.8
Pt/γ-Al$_2$O$_3$	144	11	0.39	1.9	1.0
Pt/5SiO$_2$–95Al$_2$O$_3$	266	7	0.60	1.5	0.7
Pt/30SiO$_2$–70Al$_2$O$_3$	315	8	0.64	1.8	0.5
Pt/ZrO$_2$	42	19	0.21	2.1	0.7
Pt/CeO$_2$–ZrO$_2$	70	14	0.24	1.6	0.5
Pt/Nb$_2$O$_5$	73	6	0.13	2.0	0.5
Pt/TiO$_2$	100	13	0.25	1.7	0.6

This journal is © The Royal Society of Chemistry 2024

Catal. Sci. Technol., 2024, **14**, 431–448 | **435**

3. Results

3.1 Catalyst characterization

Table 1 displays the specific surface area, mean pore diameter and pore volume obtained from N_2-physisorption measurements, as well as the mean Pt particle size and standard deviation of the mean Pt particle size derived from STEM images.

There was considerable variability between the specific surface area, pore volume, and pore size distribution of the catalysts (Table 1). The specific surface area increased in the order of Pt/ZrO$_2$ (42 m^2 g^{-1}) < Pt/CeO$_2$–ZrO$_2$ (70 m^2 g^{-1}), Pt/Nb$_2$O$_5$ (73 m^2 g^{-1}) < Pt/TiO$_2$ (100 m^2 g^{-1}) < Pt/γ-Al$_2$O$_3$ (144 m^2 g^{-1}) $\ll$ Pt/5SiO$_2$–95Al$_2$O$_3$ (266 m^2 g^{-1}), Pt/SiO$_2$ (289 m^2 g^{-1}), Pt/30SiO$_2$–70Al$_2$O$_3$ (315 m^2 g^{-1}). The pore volumes increased in a similar order, with the exception of Pt/Nb$_2$O$_5$, which had the lowest pore volume (0.13 cm^3 g^{-1}). The pore volumes of Pt/5SiO$_2$–95Al$_2$O$_3$ (0.60 cm^3 g^{-1}) and Pt/30SiO$_2$–70Al$_2$O$_3$ (0.64 cm^3 g^{-1}) were also lower compared with Pt/SiO$_2$ (0.92 cm^3 g^{-1}), despite a similar surface area. Consequently, Pt/Nb$_2$O$_5$, Pt/5SiO$_2$–95Al$_2$O$_3$ and Pt/30SiO$_2$–70Al$_2$O$_3$ had the narrowest mean pore diameter (6–8 nm), while Pt/ZrO$_2$ had the largest mean pore diameter (19 nm). Fig. S2 and S3 of the ESI† display the N_2-physisorption isotherms and the BJH pore size distribution of the measured catalysts. The N_2-physisorption isotherms of all catalysts corresponded to type IV(a) of the IUPAC classification.[43]

The semi-quantitative XRF measurements provided a Pt loading of 0.6 wt% for Pt/ZrO$_2$, Pt/5SiO$_2$–95Al$_2$O$_3$ and Pt/30SiO$_2$–70Al$_2$O$_3$, while the Pt loading was 0.7 wt% for Pt/SiO$_2$ and Pt/γ-Al$_2$O$_3$, and 0.8 wt% for Pt/CeO$_2$–ZrO$_2$, Pt/Nb$_2$O$_5$ and Pt/TiO$_2$. These values are within the measurement accuracy of each other. The STEM images suggested that the Pt distribution was heterogeneous on the analyzed catalysts (Fig. S4 of the ESI†). The Pt particle size distribution derived from the STEM images is presented in Fig. S5 of the ESI.† The mean Pt particle size ranged between 1.5 and 2.1 nm for the catalysts, but the statistical significance of the differences between the mean Pt particle size of the catalysts was limited (Table 1). No reflections characteristic of Pt were identified in the X-ray diffractograms of the catalysts, which suggests that

the Pt was X-ray amorphous and well dispersed, in agreement with the STEM images (Fig. S6, ESI†).[44]

XPS measurements were carried out to study the chemical composition of the surface of the supported Pt catalysts. The catalyst samples were reduced *ex situ* at 350 °C before the measurements and transferred to the equipment through air. Table 2 presents the surface concentration of Pt, the relative fraction of the different oxidation states of Pt, the binding energy of the Pt 4f$_{7/2}$ component of Pt(0), and the binding energy of the lattice oxygen for all catalysts. Fig. 1 displays the Pt 4f/Al 2p region for all catalysts. The survey spectra of all catalysts are available in Fig. S7 of the ESI,† and the surface elemental composition of the catalysts is presented in Table S1 of the ESI.†

As seen from Table 2 and Fig. 1, shifts up to 0.5 eV were identified between the Pt(0) binding energies of the catalysts, potentially indicative of differences in electron transfer between Pt and the supports. Pt/TiO$_2$ displayed the lowest Pt 4f binding energy, *i.e.*, the highest electron density for Pt, whereas Pt/Nb$_2$O$_5$ had the highest Pt 4f binding energy. The oxidation state of Pt was similar for all catalysts, and most of the platinum, 69–82%, was in the form of metallic Pt(0). Pt(I) was the second most prevalent oxidation state, 11–17%, for all catalysts except for Pt/γ-Al$_2$O$_3$, followed by less than 6% in each of the higher oxidation states. Out of the measured catalysts, Pt/γ-Al$_2$O$_3$ displayed the highest amount of Pt at higher oxidation states and had the highest concentration of the mixed Pt state, 15%. The surface concentration of Pt varied between 3.2 and 6.2 at%.

As expected, the O 1s lattice oxygen binding energies differed significantly between the catalysts (Table 2). Pt/TiO$_2$, Pt/ZrO$_2$ and Pt/CeO$_2$–ZrO$_2$ exhibited the lowest lattice oxygen binding energies (529.6–530.0 eV), followed by Pt/Nb$_2$O$_5$ (530.3 eV), and Pt/γ-Al$_2$O$_3$, Pt/5SiO$_2$–95Al$_2$O$_3$ and Pt/30SiO$_2$–70Al$_2$O$_3$ (531.5–531.7 eV). Pt/SiO$_2$ had the highest lattice oxygen binding energy, 533.4 eV.

The characteristics of the Al 2p and Al 2s peaks of Pt/γ-Al$_2$O$_3$, Pt/5SiO$_2$–95Al$_2$O$_3$ and Pt/30SiO$_2$–70Al$_2$O$_3$ were similar, with energies corresponding to Al$_2$O$_3$. The binding energy of the Si 2p spectra of Pt/SiO$_2$, Pt/5SiO$_2$–95Al$_2$O$_3$ and Pt/30SiO$_2$–70Al$_2$O$_3$ (103.0 eV) suggests a sub-oxide state for the silica,

Table 2 XPS-derived atomic surface concentration of Pt[a], relative amounts of the different oxidation states of platinum, and the binding energies of Pt(0)[b] and the lattice O[c]

Catalyst	Pt 4f/4d[a] (at%)	Oxidation states of Pt					Binding energy	
		Pt(0) (%)	Pt(I) (%)	Pt(mix) (%)	Pt(II) (%)	Pt(IV) (%)	Pt(0)[b] (eV)	Lattice O[c] (eV)
Pt/SiO$_2$	3.4	75%	12%	3%	6%	4%	71.0	533.4
Pt/γ-Al$_2$O$_3$	5.9	69%	4%	15%	6%	6%	70.8	531.5
Pt/5SiO$_2$–95Al$_2$O$_3$	6.2	71%	15%	4%	5%	5%	71.0	531.5
Pt/30SiO$_2$–70Al$_2$O$_3$	3.6	75%	16%	1%	4%	5%	70.9	531.7
Pt/ZrO$_2$	4.9	72%	16%	3%	5%	4%	70.9	530.0
Pt/CeO$_2$–ZrO$_2$	3.9	72%	17%	2%	6%	3%	70.9	529.6
Pt/Nb$_2$O$_5$	4.5	77%	12%	2%	6%	3%	71.2	530.3
Pt/TiO$_2$	3.2	82%	11%	1%	3%	3%	70.7	530.0

[a] Pt 4d used for Pt/SiO$_2$, Pt/γ-Al$_2$O$_3$, Pt/5SiO$_2$–95Al$_2$O$_3$ and Pt/30SiO$_2$–70Al$_2$O$_3$. [b] Pt 4f$_{7/2}$. [c] O 1s.

436 | *Catal. Sci. Technol.*, 2024, **14**, 431–448

This journal is © The Royal Society of Chemistry 2024
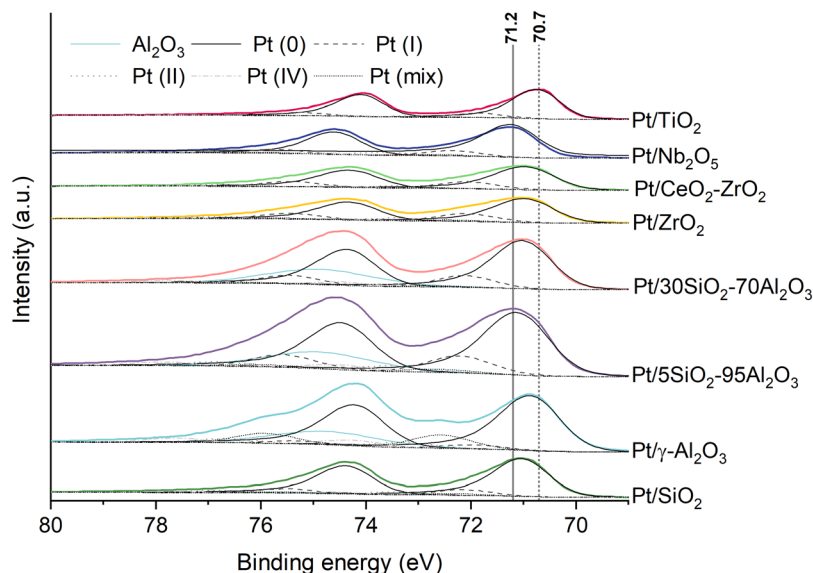
Fig. 1 High-resolution X-ray photoelectron spectra of the Pt 4f/Al 2p region of the supported Pt catalysts. The catalysts were reduced *ex situ* at 350 °C before the measurements.

and a lower $O/(1.5Al + 2Si)$ ratio was observed with increasing amounts of Si in the catalysts (Table S2, ESI†). The sub-oxide state may be related to electronic interactions between Pt and SiO_2.[45] Sodium (0.4 at%) was additionally detected on the surface of Pt/SiO_2.

Two components were identified from the Zr 3d spectra of the Pt/ZrO_2 and Pt/CeO_2–ZrO_2 catalysts, with $3d_{5/2}$ peaks located at 182.1 and 183.4 eV. The lower binding energy component corresponds to ZrO_2, while the higher binding energy component may be related to surface defects or Zr bound to hydroxyl species. Of the Zr atoms on the catalyst surface, 16.3% and 10.8% were found in the higher binding energy state for Pt/ZrO_2 and Pt/CeO_2–ZrO_2, respectively. Of the Ce atoms on the surface of Pt/CeO_2–ZrO_2, 38.5% were found as Ce(III) and 61.5% as Ce(IV), implying that reduction of the support readily occurred, and that Ce was present in both oxidation states under the reaction conditions.

The reducibility and reducible species of the bare supports and the catalysts was qualitatively studied *via* H_2-TPR. The H_2-TPR profiles are presented in Fig. 2 for the bare supports (a) and the calcined supported Pt catalysts (b).

No reducible species could be identified from the bare SiO_2, γ-Al_2O_3, $5SiO_2$–$95Al_2O_3$, $30SiO_2$–$70Al_2O_3$, ZrO_2 and Nb_2O_5 supports (Fig. 2a). The H_2-TPR profile of the bare CeO_2–ZrO_2 support had a major reduction peak with a maximum intensity at 560 °C, which based on the XPS measurements, was related to the reduction of Ce(IV) to Ce(III). The H_2 consumption was elevated in the H_2-TPR profile of the bare TiO_2 support between 350 °C and 550 °C, plateauing at 450 °C. This likely corresponded to the partial reduction of TiO_2.[46,47]

The H_2 consumption was slightly elevated until approximately 100 °C in the H_2-TPR profiles of the Pt/SiO_2, $Pt/γ$-Al_2O_3, $Pt/5SiO_2$–$95Al_2O_3$, $Pt/30SiO_2$–$70Al_2O_3$, Pt/Nb_2O_5
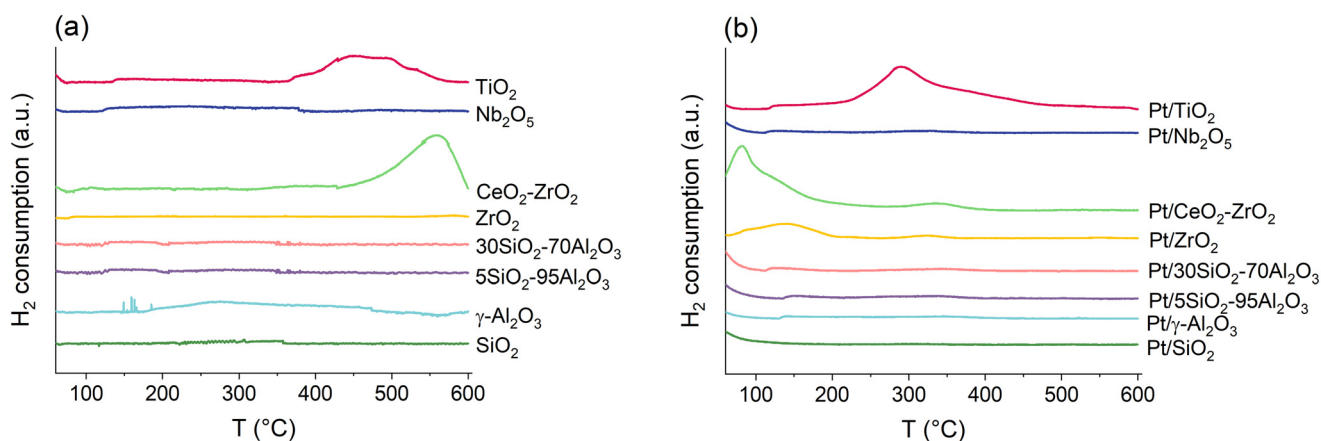
Fig. 2 H_2-TPR profiles of (a) the bare supports and (b) the calcined supported Pt catalysts.

This journal is © The Royal Society of Chemistry 2024

Catal. Sci. Technol., 2024, **14**, 431–448 | **437**

and Pt/TiO$_2$ catalysts. This can likely be attributed to the reduction of bulk PtO$_2$ species with weak interactions with the support or potentially to the chemisorption of H$_2$ (Fig. 2b).[48-50] Stabilization of the gas flow may also have been partially responsible for the elevated signal at the start of the temperature ramp. The H$_2$-TPR profiles of Pt/SiO$_2$, Pt/γ-Al$_2$O$_3$, Pt/5SiO$_2$-95Al$_2$O$_3$, Pt/30SiO$_2$-70Al$_2$O$_3$ and Pt/Nb$_2$O$_5$ contained no further peaks, suggesting that Pt was in its reduced form before the H$_2$-TPR measurement, or that the reduction occurred before 100 °C. No metal-assisted reduction of the support appeared to occur for these catalysts in the studied temperature range. For the irreducible oxides, i.e., SiO$_2$, γ-Al$_2$O$_3$, and both SiO$_2$-Al$_2$O$_3$ supports, the results align with the literature, whereas the lack of peaks related to the reduction of the support was somewhat more surprising for Pt/Nb$_2$O$_5$.[48,51-53]

The H$_2$-TPR profile of Pt/ZrO$_2$ contained a broad reduction peak with a maximum intensity at 140 °C, likely corresponding to the reduction of Pt (Fig. 2b).[30,54] The H$_2$-TPR profile of Pt/CeO$_2$-ZrO$_2$ exhibited a major reduction peak between the start of the temperature ramp and 170 °C, with a maximum intensity at 83 °C and a shoulder at approximately 120 °C (Fig. 2b). A minor reduction peak was additionally observed at 335 °C. The higher reduction temperature of Pt on Pt/ZrO$_2$ and Pt/CeO$_2$-ZrO$_2$ may indicate stronger electronic interactions between Pt and the support compared with the other catalysts.[51,55-57] The reduction peak observed at 560 °C on the bare CeO$_2$-ZrO$_2$ support (Fig. 2a) was completely absent from the H$_2$-TPR profile of the Pt/CeO$_2$-ZrO$_2$ catalyst. This suggests that the broad reduction peak on Pt/CeO$_2$-ZrO$_2$ with a maximum intensity at 83 °C involved both reduction of Pt and the support. In the literature, this has been explained by dissociative adsorption of H$_2$ on the reduced Pt particles followed by spillover to the support, which facilitates the reduction of the support.[58-62]

The H$_2$-TPR profile of the Pt/TiO$_2$ catalyst contained a major reduction peak with a maximum intensity at 290 °C, which is 160 °C lower than the maximum intensity of the reduction peak of the bare TiO$_2$ support (Fig. 2). The presence of Pt, therefore, lowered the reduction temperature

of TiO$_2$ on the Pt/TiO$_2$ catalyst, similar to Pt/CeO$_2$-ZrO$_2$.[30,55,63]

The desorbed amounts of CO$_2$ derived from the CO$_2$-TPD measurements are presented in Table 3, whereas the CO$_2$ desorption profiles are displayed in Fig. S8 of the ESI.† The CO$_2$-TPD results are indicative of the basicity of the catalysts, with the amount of adsorbed CO$_2$ describing the number of basic sites and the desorption temperature correlating with the strength of the basic sites.[64]

Overall, the catalysts displayed relatively weak basicity. The CO$_2$ desorption peak reached its maximum intensity at 105-110 °C for all catalysts (Fig. S8, ESI†). The CO$_2$ adsorption capacity of Pt/γ-Al$_2$O$_3$ and Pt/5SiO$_2$-95Al$_2$O$_3$ were similar at 26 and 22 μmol g$_{cat}^{-1}$, respectively (Table 3). The basic site concentration of SiO$_2$-Al$_2$O$_3$ materials is known to decrease markedly as the SiO$_2$ content increases, explaining the insignificant basicity of Pt/30SiO$_2$-70Al$_2$O$_3$.[65] SiO$_2$ and Nb$_2$O$_5$ likewise had a negligible CO$_2$ adsorption capacity. Slightly less CO$_2$ (15 μmol g$_{cat}^{-1}$) desorbed from Pt/TiO$_2$ than from Pt/γ-Al$_2$O$_3$ and Pt/5SiO$_2$-95Al$_2$O$_3$. The CO$_2$ adsorption capacity of Pt/ZrO$_2$ and Pt/CeO$_2$-ZrO$_2$ was the highest out of the catalysts at 42 and 210 μmol g$_{cat}^{-1}$, respectively.

Acid site characterization was performed using FTIR spectroscopy, with pyridine as the probe molecule. Fig. 3 displays the FTIR spectra of the pyridine-saturated catalyst samples, whereas the Table 3 presents the adsorbed amounts of pyridine on Lewis acid sites and Brønsted acid sites.

The catalysts displayed major differences in the acid site concentration and exhibited varying acid site strength, as observed from shifts in the wavenumber of the absorption bands (Table 3, Fig. 3).[66-68] The catalysts were predominantly Lewis acidic (1442-1453 cm^{-1}), and Brønsted acid sites were identified only on Pt/30SiO$_2$-70Al$_2$O$_3$ (1546 cm^{-1}) and Pt/Nb$_2$O$_5$ (1540 cm^{-1}). Overall, the obtained FTIR spectra and adsorbed amounts of pyridine align with those reported for similar catalysts and supports in the literature.[66-68]

The catalysts were divided into four groups based on the strength of their Lewis acid sites. The first group comprises the catalysts with the strongest Lewis acid sites, Pt/30SiO$_2$-70Al$_2$O$_3$, Pt/5SiO$_2$-95Al$_2$O$_3$ and Pt/γ-Al$_2$O$_3$. The vibration bands characteristic of pyridine adsorbed on Lewis acid sites
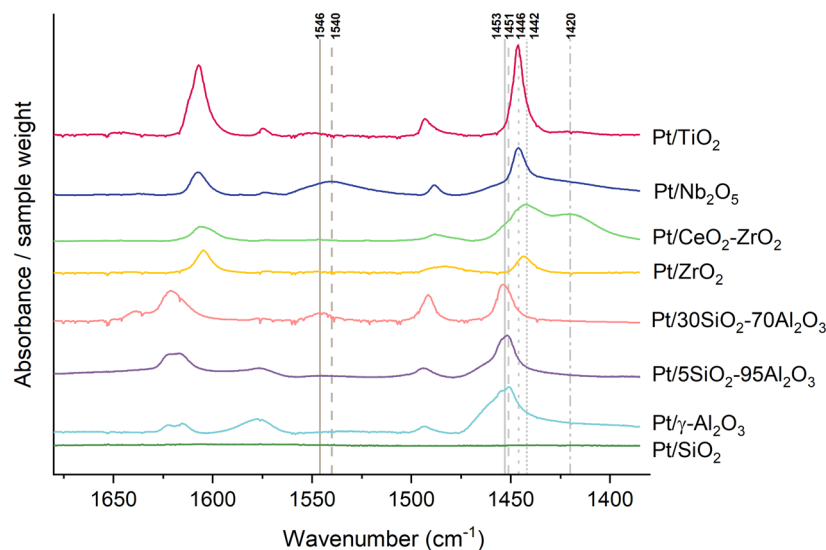
Table 3 The concentration of acid sites and basic sites of the Pt catalysts, obtained via FTIR spectroscopy using pyridine as a probe molecule and from CO$_2$-TPD measurements, respectively

Catalyst	Lewis acidity[a] (μmol g^{-1})	Brønsted acidity[a] (μmol g^{-1})	Total acidity[a] (μmol g^{-1})	Total basicity[b] (μmol g^{-1})	Lewis acidity[a] (μmol m^{-2})	Brønsted acidity[a] (μmol m^{-2})	Total acidity[a] (μmol m^{-2})	Total basicity[b] (μmol m^{-2})
Pt/SiO$_2$	~0	~0	~0	2	~0	~0	~0	<0.1
Pt/γ-Al$_2$O$_3$	210	~0	210	26	1.4	~0	1.8	0.2
Pt/5SiO$_2$-95Al$_2$O$_3$	150	~0	150	22	0.6	~0	0.6	0.1
Pt/30SiO$_2$-70Al$_2$O$_3$	70	30	100	3	0.2	0.1	0.3	<0.1
Pt/ZrO$_2$	30	~0	30	42	0.7	~0	0.7	0.8
Pt/CeO$_2$-ZrO$_2$	240	~0	240	210	3.4	~0	3.4	3.0
Pt/Nb$_2$O$_5$	210	90	300	2	2.8	1.3	4.1	<0.1
Pt/TiO$_2$	140	<10	140	15	1.4	<0.1	1.4	0.2

[a] From FTIR spectroscopy using pyridine as a probe molecule. [b] From CO$_2$-TPD measurements.

438 | Catal. Sci. Technol., 2024, **14**, 431-448

This journal is © The Royal Society of Chemistry 2024

Fig. 3 Transmission FTIR spectra for the pyridine-saturated supported Pt catalysts, with the background and spectra of the clean samples subtracted. The spectra were collected at 170 °C. The vibration bands characteristic for pyridine adsorbed on Brønsted acid sites (1540 and 1546 cm^{-1}) and Lewis acid sites (1442–1453 cm^{-1}) have been indicated with vertical lines.

were located at 1453 cm^{-1} for Pt/30SiO$_2$–70Al$_2$O$_3$ and at 1451 cm^{-1} for Pt/5SiO$_2$–95Al$_2$O$_3$ and Pt/γ-Al$_2$O$_3$ (Fig. 3).[66–68] In the following, this group is referred to as Si–Al. In the case of Pt/Nb$_2$O$_5$ and Pt/TiO$_2$, the vibration band of pyridine adsorbed on Lewis acid sites was shifted toward a lower wavenumber (1446 cm^{-1}) compared with the catalysts of the Si–Al group. This indicates the presence of Lewis acid sites of intermediate strength.[66–68] Pt/Nb$_2$O$_5$ and Pt/TiO$_2$, therefore, formed their own group, referred to as Ti–Nb. Pt/ZrO$_2$ and Pt/CeO$_2$–ZrO$_2$, denoted Ce–Zr, contained the weakest Lewis acid sites, with the main vibration band of pyridine adsorbed on Lewis acid sites located at 1442 cm^{-1} for both catalysts.[66–68] The FTIR spectra of Pt/CeO$_2$–ZrO$_2$ showed another vibration band at 1420 cm^{-1}, possibly attributed to hydrogen-bonded pyridine or pyridine adsorbed on weaker Lewis acid sites, e.g., Ce^{3+} cations.[68,69] Pt/SiO$_2$ was the only catalyst where no pyridine adsorption could be detected and hence formed its own group (Si).

The Lewis acid site concentration of the catalysts of the Si–Al group decreased in the order Pt/γ-Al$_2$O$_3$ (210 μmol g^{-1}, Table 3), Pt/5SiO$_2$–95Al$_2$O$_3$ (150 μmol g^{-1}), and Pt/30SiO$_2$–70Al$_2$O$_3$ (70 μmol g^{-1}). Pt/30SiO$_2$–70Al$_2$O$_3$ additionally adsorbed 30 μmol g^{-1} pyridine on Brønsted acid sites, but its total acidity remained lower compared with the other catalysts in the Si–Al group. For SiO$_2$–Al$_2$O$_3$ materials, the Lewis acidity is known to decrease and the Brønsted acidity to increase as the SiO$_2$ content increases.[65] The results are, therefore, in line with the literature.

Within the Ti–Nb group, the Lewis acid site concentration of Pt/Nb$_2$O$_5$ (210 μmol g^{-1}, Table 3) exceeded the Lewis acid site concentration of Pt/TiO$_2$ (140 μmol g^{-1}). Pt/Nb$_2$O$_5$ additionally adsorbed 90 μmol g^{-1} pyridine on weak Brønsted acid sites and therefore had the highest total acid site concentration out of the studied catalysts.[66,70] Pt/CeO$_2$–ZrO$_2$

had the highest Lewis acid site concentration (240 μmol g^{-1}) out of all tested catalysts, whereas Pt/ZrO$_2$ had the second lowest acid site concentration of the catalysts (30 μmol g^{-1}), after the non-acidic Pt/SiO$_2$.

3.2 Catalytic hydrotreatment of *n*-hexadecanamide

Hydrotreating experiments using *n*-hexadecanamide (C16 amide, 100 ppm N) as the model compound were carried out for the bare supports and the supported Pt catalysts at 300 °C and 80 bar H$_2$ for 60 min. The product samples contained *n*-pentadecane (C15 paraffin), *n*-hexadecane (C16 paraffin), *n*-hexadecanal (C16 aldehyde), 1-hexadecanol (C16 alcohol), palmitic acid (C16 acid), *n*-hexadecanonitrile (C16 nitrile), 1-hexadecylamine (C16 amine), dipentadecyl ketone (C31 ketone), *n*-hexadecyl hexadecylamine (C32 amine), palmityl palmitate (C32 ester), and *n*-hexadecyl hexadecanamide (C32 amide). Fig. 4 presents the product distribution, conversion and nitrogen removal from the C16 amide hydrotreating experiments on the bare supports (a) and supported Pt catalysts (b), grouped according to their Lewis acid site strength. The oxygen removal, estimated from the product distribution, has also been indicated for the supported Pt catalysts.

Fig. 5 displays the product distribution for the hydrotreatment of C16 amide (300 °C and 80 bar H$_2$) as a function of batch residence time for the Pt/γ-Al$_2$O$_3$ (a), Pt/TiO$_2$ (b) and Pt/ZrO$_2$ (c) catalysts, representing the Si–Al, Ti–Nb, and Ce–Zr groups, respectively. The 60 min reference experiments shown in Fig. 4 correspond to a batch residence time of 0.37 g$_{cat}$ h g$_{amide}^{-1}$.

The product distribution of the 60 min experiments was similar for the catalysts within each group, but the groups deviated from one another, especially in conversion and
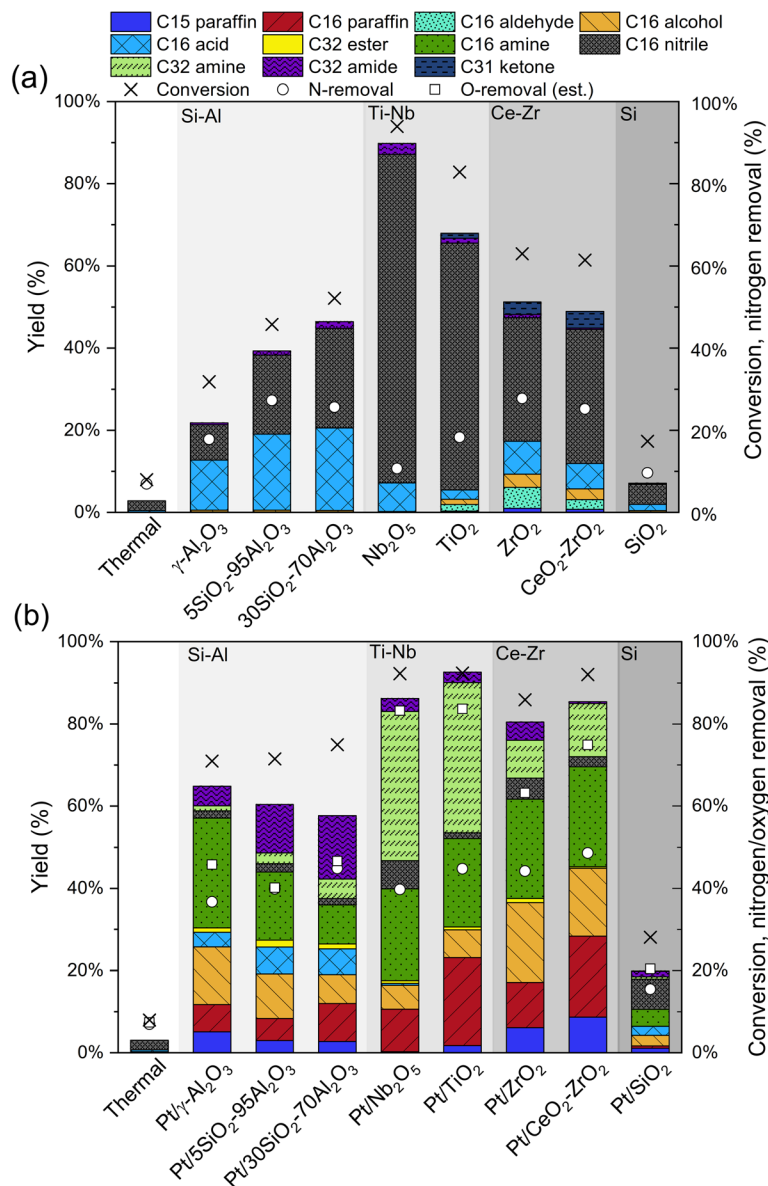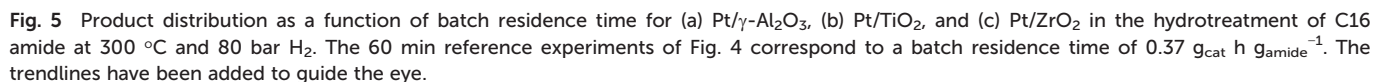
Fig. 4 Product distribution, conversion and nitrogen removal of the C16 amide hydrotreating experiments on (a) the bare supports and (b) the supported Pt catalysts. The oxygen removal of the supported Pt catalysts was derived from the product distribution, while the nitrogen removal was obtained from the total nitrogen content analysis. The materials have been grouped according to their Lewis acid site strength. Reaction conditions: 300 °C, 80 bar H_2, 60 min ($\tau = 0.37$ g_{cat} h g_{amide}^{-1}).

oxygen removal (Fig. 4). The differences in nitrogen removal and paraffin yields were initially smaller between the groups but became more pronounced with an increasing batch residence time (Fig. 5). A reaction network, adapted and extended from a previous study conducted by Verkama et al.,[16] is proposed in Scheme 1. The following paragraphs introduce the reaction network on a general level, whereas the activity and selectivity of each group are discussed in sections 3.2.1–3.2.4.

The conversion of C16 amide appeared to proceed via two main pathways on the bare supports. One main pathway comprised the bimolecular deammoniation (BDA) of C16 amide to an isoimide, which decomposed to C16 nitrile and

C16 acid (Scheme 1).[71] The BDA of amides has been described by Davidson and Karten.[71] The direct dehydration to C16 nitrile was the other main pathway for the conversion of C16 amide, and the preference between direct dehydration and BDA depended on the support. The hydrolysis of C16 amide to C16 acid and ammonia may have occurred additionally.[21,72] The BDA and dehydration of C16 amide also occurred thermally, but the thermal activity was considerably lower compared with the activity of all tested materials except for the bare SiO_2 support (Fig. 4a).[71] In the case of the supported Pt catalysts, the conversion of C16 amide might have concurrently proceeded through other pathways, such as HDN to C16 aldehyde or C16 alcohol, and HDO to C16

Fig. 5 Product distribution as a function of batch residence time for (a) Pt/γ-Al$_2$O$_3$, (b) Pt/TiO$_2$, and (c) Pt/ZrO$_2$ in the hydrotreatment of C16 amide at 300 °C and 80 bar H$_2$. The 60 min reference experiments of Fig. 4 correspond to a batch residence time of 0.37 g$_{cat}$ h g$_{amide}$$^{-1}$. The trendlines have been added to guide the eye.

imine.[18,21,25,26,73] The conversion of C16 amide to C16 alcohol and C16 imine likely proceeded *via* a hemiaminal intermediate, and C16 imine was rapidly hydrogenated further to C16 amine.[21] The isoimide, hemiaminal and imine intermediates were not detected in the product samples. Therefore, the initial pathway selectivity of the supported Pt catalysts could not be unambiguously confirmed from the experimental data. The distribution between oxygen-

containing and nitrogen-containing intermediate products was, nevertheless, similar for the supported Pt catalysts and the corresponding bare supports, which might indicate that they favored the same initial conversion routes (Fig. 4).

The bimolecular ketonization of C16 acid to C31 ketone and the reduction of C16 acid to C16 aldehyde and ultimately to C16 alcohol were observed on the bare ZrO$_2$, CeO$_2$–ZrO$_2$ and TiO$_2$ supports (Fig. 4).[15,74–76] These bare supports
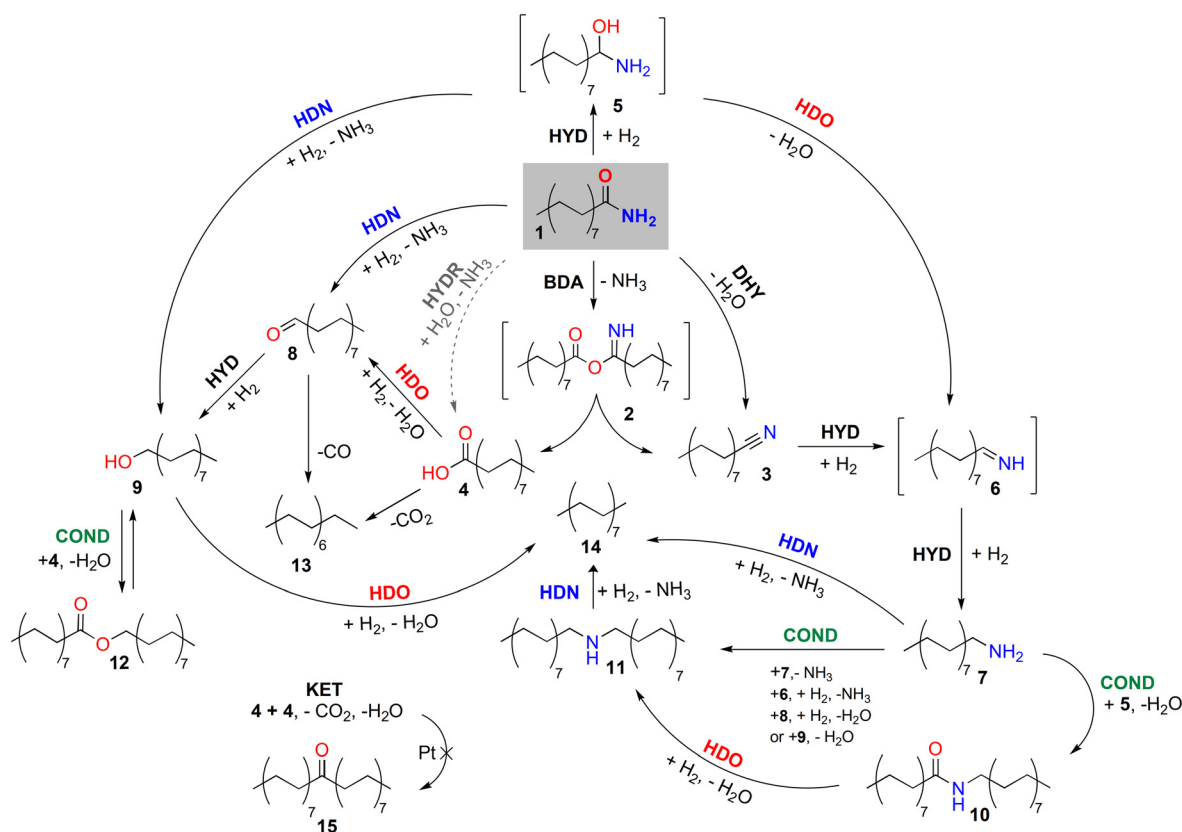
Scheme 1 Proposed reaction network for the hydrotreatment of C16 amide. Indicated compounds: **1** C16 amide, **2** C32 isoimide, **3** C16 nitrile, **4** C16 acid, **5** C16 hemiaminal, **6** C16 imine, **7** C16 amine, **8** C16 aldehyde, **9** C16 alcohol, **10** C32 amide, **11** C32 amine, **12** C32 ester, **13** C15 paraffin, **14** C16 paraffin, and **15** C31 ketone. The bimolecular deammoniation (BDA), direct dehydration (DHY), hydrogenation (HYD) and hydrolysis (HYDR) of the C16 amide, and the condensation (COND), HDO and HDN reactions of the intermediates have been indicated. The bimolecular ketonization of the C16 acid (KET) only occurred over the bare supports. The reaction network has been adapted and extended from a previous study conducted by Verkama *et al.*[16]

This journal is © The Royal Society of Chemistry 2024

Catal. Sci. Technol., 2024, **14**, 431–448 | **441**

showed the lowest carbon balance closure (~85%) out of all tested materials, which might indicate that some reaction products remained adsorbed on the supports or that non-volatile products that could not be detected with the GC were formed, additionally. C16 aldehyde and C31 ketone were not present in the product samples of the supported Pt catalysts.

C16 nitrile, C16 acid, C16 aldehyde, C16 alcohol, and C16 amine were further converted over all of the supported Pt catalysts, eventually forming C15 paraffin and C16 paraffin (Scheme 1, Fig. 4). C16 nitrile was readily hydrogenated to C16 amine, whereas C16 acid was hydrogenated to C16 alcohol, either directly or *via* C16 aldehyde.[32] C15 paraffin was formed *via* decarboxylation of C16 acid and decarbonylation of C16 aldehyde, while C16 paraffin was obtained from the HDO of C16 alcohol and the HDN of C16 amine. C32 amine, C32 amide and small amounts of C32 ester were formed *via* condensation reactions of the intermediates, as indicated in Scheme 1 and discussed by Verkama *et al.*[16] For instance, C32 amide was formed through the condensation of C16 acid and C16 amine.[16,32] The C32 condensation products eventually decomposed to C16 paraffin.[16,77,78]

3.2.1 Activity of the Si–Al group. The bare supports of the Si–Al group favored the conversion of C16 amide *via* BDA, as indicated by the stoichiometric formation of C16 acid and C16 nitrile (Fig. 4a, Scheme 1). Considering the presence of C16 acid and C16 nitrile in the product samples of the supported Pt catalysts, and the similar distribution between oxygen-containing and nitrogen-containing intermediate products, it is possible that the BDA pathway was favored on the supported Pt catalysts of the Si–Al group as well (Fig. 4b). However, given the prominence of C16 amine and C16 alcohol at the lowest studied batch residence times, the concurrent conversion of C16 amide to C16 amine and C16 alcohol cannot be excluded (Fig. 5a). In the 60 min reference experiments, Pt/γ-Al$_2$O$_3$, Pt/5SiO$_2$–95Al$_2$O$_3$ and Pt/30SiO$_2$–70Al$_2$O$_3$ all reached approximately 70% C16 amide conversions and removed between 37% and 45% of nitrogen and similar amounts of oxygen (Fig. 4b). Pt/30SiO$_2$–70Al$_2$O$_3$ was the most active out of the catalysts of the Si–Al group, but the difference compared to Pt/γ-Al$_2$O$_3$ and Pt/5SiO$_2$–95Al$_2$O$_3$ was subtle.

The supported Pt catalysts of the Si–Al group were highly active for the formation of C16 amine through hydrogenation of C16 nitrile (Fig. 4b). In the batch residence time series experiments on Pt/γ-Al$_2$O$_3$, this was reflected by C16 amine dominating the nitrogen-containing intermediates, whereas the C16 nitrile yield never exceeded 2% (Fig. 5a). The HDO of C16 acid, in contrast, proceeded relatively slowly over the supported Pt catalysts of the Si–Al group, as indicated by high yields of C16 acid in the product samples of the 60 min reference experiments (Fig. 4b). Consequently, C16 acid and C16 amine were present in relatively high amounts, which favored the formation of C32 amide (Scheme 1).[16] In particular, the Pt/SiO$_2$–Al$_2$O$_3$ catalysts showed a high tendency towards the formation of C32 amide (12–15%). C32

amine was also formed, but to a lower extent than on the other groups. In the batch residence time series experiments on Pt/γ-Al$_2$O$_3$, the C32 amide and C32 amine yields first increased and then stabilized (Fig. 5a). Therefore, the decomposition of these C32 compounds to C16 paraffin did not occur readily.

The total paraffin yields from the 60 min reference experiments ranged between 8% and 12% for the supported Pt catalysts of the Si–Al group (Fig. 4b). At batch residence time point 1.86 g$_{cat}$ h g$_{amide}^{-1}$, the product mixture of Pt/γ-Al$_2$O$_3$ contained 39% C16 paraffin and 12% C15 paraffin (C16 paraffin/C15 paraffin = 3.2 mol/mol, Fig. 5a). The HDO and HDN routes, therefore, dominated over decarbonylation and decarboxylation (Scheme 1).

3.2.2 Activity of the Ti–Nb group. The conversion of C16 amide exceeded 90% on Pt/Nb$_2$O$_5$ and Pt/TiO$_2$ in the 60 min reference experiments, whereas the nitrogen removals were 39% and 45%, respectively (Fig. 4b). Based on the product distributions, the oxygen removal exceeded the nitrogen removal by approximately 40 percentage points on the supported Pt catalysts of the Ti–Nb group, indicating that the group was highly active for HDO reactions. Compared with the Si–Al group, the C16 amide conversion and oxygen removal of the Ti–Nb group were, therefore, around 20 and 40 percentage points higher, respectively, whereas the nitrogen removal was similar. The bare support tests confirmed these trends.

The high yields of C16 nitrile (60–80%) and low yields of C16 acid (<10%) on the bare supports of the Ti–Nb group indicate that C16 amide was primarily converted through direct dehydration (Fig. 4a, Scheme 1). The strong tendency towards the oxygen removal from C16 amide was reflected by C16 and C32 amines dominating the product distribution of the supported Pt catalysts of the Ti–Nb group (Fig. 4b). Notably, the yield of C32 compounds in the product samples of the reference experiments was 2–3 times higher for the supported Pt catalysts of the Ti–Nb group compared with the other catalysts. However, the steep decrease in the C32 amine yield on Pt/TiO$_2$ at batch residence times above 0.75 g$_{cat}$ h g$_{amide}^{-1}$ indicated that the catalyst was active for the conversion of C32 amine to C16 paraffin, in contrast to Pt/γ-Al$_2$O$_3$ (Fig. 5a and b).

Considerably less oxygen-containing intermediate products (<10%) were present in the product samples of the Ti–Nb group compared with the other groups (Fig. 4a and b). All oxygen-containing compounds were converted with a batch residence time of 0.75 g$_{cat}$ h g$_{amide}^{-1}$ on Pt/TiO$_2$, further reflecting the high HDO activity (Fig. 5b).

Pt/TiO$_2$ showed a total paraffin yield of 23% in the 60 min reference experiment, which exceeded the paraffin yields of the Si–Al group and Pt/Nb$_2$O$_5$ (10%) significantly (Fig. 4b). The Ti–Nb group favored C16 paraffin over C15 paraffin to an even greater extent than the Si–Al group, *i.e.*, no C15 paraffin was detected for Pt/Nb$_2$O$_5$, and the C15 paraffin yield was below 2% for Pt/TiO$_2$. At the highest batch residence time point (1.86 g$_{cat}$ h g$_{amide}^{-1}$), the total paraffin yield of Pt/

442 | *Catal. Sci. Technol.*, 2024, **14**, 431–448

This journal is © The Royal Society of Chemistry 2024

TiO$_2$ was 80% (23 mol$_{C16\ paraffin}$/mol$_{C15\ paraffin}$), which is 26 percentage points higher than the total paraffin yield of Pt/γ-Al$_2$O$_3$ at a similar batch residence time (Fig. 5a and b).

3.2.3 Activity of the Ce–Zr group. The Ce–Zr group converted the C16 amide to oxygen-containing and nitrogen-containing intermediate products with a similar selectivity as the Si–Al group, but the conversion, HDN activity and HDO activity were higher than in the Si–Al group (Fig. 4). In the 60 min reference experiments, Pt/ZrO$_2$ converted 87% of the C16 amide and removed 45% of the nitrogen, while Pt/CeO$_2$–ZrO$_2$ converted 92% of C16 amide and removed 49% of the nitrogen (Fig. 4b). The oxygen removal exceeded the nitrogen removal by 20–25 percentage points for both catalysts.

The conversion of the oxygen-containing intermediates proceeded more efficiently on the Ce–Zr group than on the Si–Al group. In the bare support experiments, this was reflected by the Ce–Zr group exhibiting activity towards the reduction and ketonization of C16 acid to C16 aldehyde and C31 ketone, respectively (Fig. 4a). For the supported Pt catalysts, the enhanced HDO activity of the Ce–Zr group could be observed, e.g., based on the absence of C16 acid in the product samples of the 60 min reference experiments (Fig. 4b), and upon comparing the evolution of the C16 acid and C16 alcohol yields in the batch residence time series experiments (Fig. 5a and c).

Pt/CeO$_2$–ZrO$_2$ formed 11 percentage points more paraffins (28%) than Pt/ZrO$_2$ in the 60 min reference experiment (Fig. 4b). Considering the overall product distribution, conversion, nitrogen removal and oxygen removal, Pt/CeO$_2$–ZrO$_2$ was more active than Pt/ZrO$_2$ in both HDN and HDO, even though the corresponding bare supports exhibited a similar activity level (Fig. 4a).

In a similar way to the other supported Pt catalysts, the supported Pt catalysts of the Ce–Zr group favored C16 paraffin over C15 paraffin. The total paraffin yield of the product sample of Pt/ZrO$_2$ at the highest batch residence time (1.86 g$_{cat}$ h g$_{amide}^{-1}$) was 20 percentage points higher compared with Pt/γ-Al$_2$O$_3$ but 9 percentage points lower compared with Pt/TiO$_2$ (Fig. 5). The C16 to C15 paraffin ratio for the product sample of Pt/ZrO$_2$ was 6.1 mol/mol at this batch residence time.

Both Pt/ZrO$_2$ and Pt/CeO$_2$–ZrO$_2$ produced a total of 16% of C32 condensation products in the 60 min reference experiments. In contrast to the Si–Al group, C32 amine was present in higher quantities than C32 amide (Fig. 4b). The high activity towards the HDO of C16 acid likely limited the formation of C32 amide on the Ce–Zr group, whereas the formation of C32 amine via condensation of C16 alcohol and C16 amine was more preferred (Scheme 1).[16] C32 amine could be further converted to C16 paraffin, but this was not favored until the oxygen-containing intermediates had been consumed (Fig. 5c).[16]

3.2.4 Activity of the Si group. The activity of the Si group was inferior compared with the other groups, but the selectivity was similar to the Si–Al group (Fig. 4). The C16 acid and C16 nitrile yields on the bare SiO$_2$ support (<5%)

were only 3 percentage points higher compared with the thermal test. Pt/SiO$_2$, in turn, converted 30% of the C16 amide and removed 15% of the nitrogen and was, therefore, less active than the bare supports of the other groups.

4. Discussion

The Si–Al (Pt/γ-Al$_2$O$_3$, Pt/5SiO$_2$–95Al$_2$O$_3$, Pt/30SiO$_2$–70Al$_2$O$_3$), Ti–Nb (Pt/TiO$_2$, Pt/Nb$_2$O$_5$), Ce–Zr (Pt/ZrO$_2$, Pt/CeO$_2$–ZrO$_2$), and Si (Pt/SiO$_2$) groups exhibited clear differences in their activity and selectivity for the HDO and HDN of C16 amide. The following sections discuss the impact of the material properties on the initial C16 amide conversion route, HDO activity, HDN activity, and the role of the C32 compounds in the reaction network.

4.1 Initial conversion pathway

The selectivity towards the initial C16 amide conversion route differed between the catalyst groups (Fig. 4 and 5). On the bare supports, the main pathways were the direct dehydration of C16 amide to C16 nitrile and the BDA of C16 amide to C16 acid and C16 nitrile, whereas the supported Pt catalysts additionally may have converted the C16 amide to C16 alcohol and C16 amine via HDN and HDO, respectively (Scheme 1).

The Ti–Nb group was highly active for the initial oxygen removal from C16 amide; thus, the nitrogen-containing intermediates dominated the product distribution. The significant initial C16 nitrile yields suggest that the direct dehydration of C16 amide was favored both on the bare supports and the supported Pt catalysts (Fig. 4 and 5b). Based on the product distribution, the HDO of C16 amide to C16 amine could nevertheless not be excluded on the supported Pt catalysts. The direct dehydration reaction was likely initiated upon the adsorption of the amide carbonyl group on the intermediate strength Lewis acid sites of TiO$_2$ and Nb$_2$O$_5$.[72,79] Shimizu et al.[18] found that the oxygen of the carbonyl group of acetamide interacted more strongly with the Lewis acid sites of Nb$_2$O$_5$ and MoO$_3$/TiO$_2$ compared with the Lewis acid sites of Al$_2$O$_3$ and ZrO$_2$, which enabled the HDO of amides to proceed efficiently on Pt/Nb$_2$O$_5$ and Pt/MoO$_3$/TiO$_2$ catalysts. These findings are in agreement with the activity of the Ti–Nb group for the initial oxygen removal from C16 amide.

In contrast, the bare supports of the Si–Al, Ce–Zr, and Si groups preferentially converted C16 amide via BDA, as indicated by the nearly stoichiometric formation of C16 nitrile and C16 acid or C16 acid derivatives (Fig. 4).[71] Based on the batch residence time series experiments, the formation of C16 amine and C16 alcohol via the HDO and HDN of C16 amide, respectively, may have occurred in parallel with BDA on the supported Pt catalysts (Fig. 5). Therefore, various oxygen-containing and nitrogen-containing intermediate products were formed on the Si–Al, Ce–Zr, and Si groups, in contrast to the Ti–Nb group, which

This journal is © The Royal Society of Chemistry 2024

Catal. Sci. Technol., 2024, **14**, 431–448 | **443**

heavily favored the nitrogen-containing intermediate products.

The conversion of C16 amide to C16 alcohol and C16 amine may have proceeded *via* the formation of a hemiaminal intermediate by a cooperative mechanism with activation of the amide carbonyl group by a Lewis acid site on the support and hydrogenation by Pt.[18,21,28,80] The enhanced conversion on the Ce–Zr group compared with the Si–Al group might therefore be related to the weak Lewis acid sites of the Ce–Zr group facilitating the formation of a hemiaminal, whereas the low activity on the Si group can be explained by the lack of Lewis acid sites (Fig. 3 and 4, Table 3). The conversion of the hemiaminal intermediate to C16 alcohol and C16 amine was likely catalyzed by the Pt sites, as the Si, Si–Al, and Ce–Zr groups exhibited a similar selectivity, despite differences in acidity and reducibility (Fig. 2).[28]

4.2 Conversion of the oxygen-containing intermediate products

The oxygen-containing intermediate products were readily formed on the Ce–Zr and Si–Al groups. However, the Ce–Zr group converted them more efficiently (Fig. 4b and 5). Therefore, the enhanced HDO activity of the Ce–Zr group distinguished the Si–Al and Ce–Zr groups from each other.

C16 acid and C16 alcohol were the most important oxygen-containing intermediate products in the reaction network of C16 amide. The HDO of C16 acid to C16 alcohol likely occurred through the adsorption of C16 acid onto the Lewis acid sites of the supports and hydrogenolysis catalyzed by Pt.[14,29,32] The HDO of C16 alcohol to the C16 paraffin may have proceeded similarly or through dehydration *via* an E2 mechanism involving Lewis acid–base site pairs (Table 3) followed by Pt-catalyzed hydrogenation.[81–83] The adsorption and dehydration of C16 alcohol may alternatively have occurred on Brønsted acid sites in the case of Pt/30SiO$_2$–70Al$_2$O$_3$. The Brønsted acidity of Pt/30SiO$_2$–70Al$_2$O$_3$ likely enhanced the dehydration activity of the catalyst, which may explain why its paraffin yield was higher compared with Pt/γ-Al$_2$O$_3$ and Pt/5SiO$_2$–95Al$_2$O$_3$ (Fig. 4b).[33,84] Nevertheless, the activity of Pt/30SiO$_2$–70Al$_2$O$_3$ did not exceed the activity of the catalysts of the Ce–Zr group.

The high HDO activity of the Ce–Zr group can be explained by the catalytic properties of the weak Lewis acid sites on Pt/ZrO$_2$ and Pt/CeO$_2$–ZrO$_2$ (Fig. 3–5). These weak Lewis acid sites can be oxophilic incompletely coordinated Zr or Ce cations.[29,85–90] Pt/CeO$_2$–ZrO$_2$ was more active than Pt/ZrO$_2$, which, considering the H$_2$-TPR, XPS, and pyridine FTIR analysis, may be due to the enhanced reducibility of the support and higher concentration of Lewis acid sites (Fig. 2, Table 3). The smaller mean Pt particle size of Pt/CeO$_2$–ZrO$_2$, *i.e.*, enhanced active surface area, may additionally explain why the catalyst was more active than Pt/ZrO$_2$ (Table 1).

The bare supports of the Si–Al group did not convert the C16 acid further. In contrast, the bare supports of the Ce–Zr

group exhibited activity for the reduction of C16 acid to C16 aldehyde and subsequent conversion to C16 alcohol (Scheme 1, Fig. 4a). The bimolecular ketonization of C16 acid to C31 ketone was also observed. The activity towards these reactions can be attributed to the Lewis acid–base and redox properties of the bare supports of the Ce–Zr group.[64,74–76,91,92] The reduction of C16 acid to C16 aldehyde was likely catalyzed by the oxygen vacancies on the ZrO$_2$ and CeO$_2$–ZrO$_2$ supports.[75,93–96] The conversion of C16 aldehyde to C16 alcohol may have been catalyzed by the Lewis acid–base site pairs of ZrO$_2$ and CeO$_2$–ZrO$_2$, which are capable of heterolytic dissociation of H$_2$.[64,91,96,97] The presence of Pt, however, markedly increased the activity towards the conversion of C16 acid to C16 alcohol (Fig. 4b). The ketonization reaction was likely Lewis acid catalyzed.[74,92]

The C15 paraffin yields of the Si–Al and Ce–Zr groups did not exceed 12% at full C16 amide conversion (Fig. 4b and 5). C15 paraffin could be formed *via* decarbonylation of C16 aldehyde or *via* decarboxylation of C16 acid, both catalyzed by Pt.[14,98] No correlation between the support or the Pt-related properties and the C15 paraffin yield were identified for the supported Pt catalysts of the Si–Al and Ce–Zr groups (Tables 1 and 2).

In contrast to the Ce–Zr and Si–Al groups, the Ti–Nb group formed relatively low amounts of oxygen-containing intermediate products due to the high initial activity for the HDO of C16 amide (Fig. 4). The low C15 paraffin selectivity of the Ti–Nb group was a consequence, as C15 paraffin was formed only from C16 acid or C16 aldehyde (Scheme 1).

4.3 Conversion of the nitrogen-containing intermediate products

The differences in the HDN activity of the catalysts were less pronounced than the differences in the HDO activity (Fig. 4). The HDN of nitrogen-containing intermediates was inhibited by the preferential HDO of oxygen-containing intermediates and the formation of condensation products.[16] Therefore, in this complex reaction network (Scheme 1), the effect of the support on the HDN activity appeared to be outweighed by the effect of the support on the initial C16 amide conversion route and HDO activity.

The hydrogenation of C16 nitrile to C16 amine was catalyzed by Pt, and all supported Pt catalysts exhibited a high activity towards the reaction (Fig. 4b and 5).[99,100] The HDN of C16 amine to C16 paraffin likely occurred *via* a mechanism involving the dissociative adsorption of C16 amine to a hydrogen-deficient surface species on the Pt sites.[13,77,101,102] A cooperative mechanism with adsorption of C16 amine on a Lewis acid site and hydrogenolysis catalyzed by Pt, similar to the HDO of C16 alcohol, may also be possible. Brønsted acid site catalyzed Hofmann elimination of C16 amine to an olefin, followed by hydrogenation of the olefin on Pt, may have occurred in the case of Pt/30SiO$_2$–70Al$_2$O$_3$ (Fig. 3).[103]

Cattenot et al.[13] suggested that the support can influence the activity and selectivity for the HDN of amines by affecting the electronic properties of the Pt particles. Based on the XPS analysis, the largest difference between the Pt electron densities was between the two catalysts of the Ti–Nb group, with Pt/TiO_2 displaying the highest and Pt/Nb_2O_5 the lowest electron density for Pt (Table 2). The selectivity of Pt/TiO_2 and Pt/Nb_2O_5 was similar, but Pt/TiO_2 showed a higher nitrogen removal and paraffin yield than Pt/Nb_2O_5 in the 60 min reference activity test (Fig. 4b). It is possible that the electronic properties of the Pt particles contributed to the enhanced HDN activity of Pt/TiO_2, but the smaller mean Pt particle size on Pt/TiO_2 than Pt/Nb_2O_5 (Table 1) may also have influenced the order of activity. No evident correlation emerged between the Pt properties and the HDN activity of the other catalysts, possibly due to the complex reaction network.

Nitrogen-containing compounds, such as amines and ammonia, can poison Lewis and Brønsted acid sites.[11,104] Strong adsorption of the C16 and C32 amines on Lewis (or Brønsted) acid sites might have interfered with the preferred reaction pathways and inhibited the catalytic activity towards the Lewis (or Brønsted) acid site catalyzed reactions. The adsorption of the nitrogen-containing intermediate products may have been stronger on the catalysts with the strongest Lewis acid sites.[11] This provides another potential explanation for the relatively low overall activity of the catalysts of group Si–Al (Fig. 3 and 4).

4.4 C32 condensation products

The formation and decomposition of the C32 condensation products played an important part in the reaction network of the supported Pt catalysts. The preference for the formation of C32 amide and C32 amine was influenced by the distribution between the oxygen-containing and the nitrogen-containing intermediate products, which in turn was determined by the initial C16 amide conversion route and the HDO activity of the catalysts. Consequently, the role of C32 amide and C32 amine in the reaction network of the Si–Al, Ti–Nb, and Ce–Zr groups differed, as discussed further in the following paragraphs.

The highest amounts of C32 amine were formed on the Ti–Nb group (Fig. 4b and 5). This may have followed from the high concentrations of C16 nitrile and C16 amine, as Pt is highly active for the formation of secondary amines via the disproportionation of primary amines and the condensation of imines and primary amines (Scheme 1).[12,13,100,102,105–107] In the case of the Ce–Zr group, C32 amine was of importance, too, but its formation through condensation of C16 alcohol and C16 amine was more favored than on the Ti–Nb group due to the significant intermediate C16 alcohol yields.[108,109]

The formation of C32 amine could be catalyzed by the Pt sites, but a mechanism involving both Pt sites and Lewis acid sites of the support may also have been possible, particularly for the pathways that involved C–O bond scission (Scheme 1).[13,32,101,107,110] The HDO activity of the weak Lewis acid sites of the Ce–Zr group might thus explain why the C32 amine was formed to a higher extent over the Ce–Zr than Si–Al group (Fig. 4b and 5).

The Si–Al group favored the formation of C32 amide over C32 amine (Fig. 4b). C32 amide was formed via condensation of C16 acid and C16 amine, and the reaction could be catalyzed by the bare supports, as observed previously by Verkama et al.[16] The C16 amine and C16 acid were likely adsorbed on Lewis or Brønsted acid sites, which was followed by a condensation reaction. The high C32 amide yield of the Si–Al group was related to the relatively high concentration of C16 acid compared with the other catalysts, which resulted from the poor HDO activity of this group.

The decomposition of the C32 compounds eventually accounted for a significant share of the C16 paraffin yield. The HDO of C32 amide to C32 amine involved Lewis acid and Pt sites.[18,80] Similarly to the HDO of C16 acid and C16 alcohol, the HDO of C32 amide proceeded efficiently over the supported Pt catalysts of the Ce–Zr and Ti–Nb groups (Fig. 4b and 5). A poor activity for the HDO of C32 amide also inhibited HDN, as the compound had to undergo HDO before its nitrogen could be removed.[78]

The HDN of C32 amine to C16 paraffin could proceed on the Pt sites, or possibly the Lewis acid and Pt sites.[13,77] The HDN of C32 amine did not seem to occur readily until the oxygen-containing intermediates had been converted, suggesting that the presence of oxygen-containing compounds inhibited the reaction (Fig. 5).[16] Consequently, the HDN of C32 amine occurred more efficiently on the Ti–Nb and Ce–Zr groups compared with the Si–Al group, which was reflected by the slow evolution of the C16 paraffin yield and accumulation of C32 compounds on $Pt/\gamma-Al_2O_3$ compared with Pt/ZrO_2 and Pt/TiO_2 (Fig. 5). These trends further emphasize the importance of the Lewis acid properties of the supports, which accounted for the differences in HDO activity.

5. Conclusions

In this study, the catalytic hydrotreatment of C16 amide (n-hexadecanamide) was studied over Pt supported on SiO_2, $\gamma-Al_2O_3$, $5SiO_2–95Al_2O_3$, $30SiO_2–70Al_2O_3$, ZrO_2, $CeO_2–ZrO_2$, Nb_2O_5 and TiO_2. The HDO and HDN of C16 amide proceeded through several parallel and competing reaction pathways. The bare supports exhibited activity for the conversion of C16 amide to C16 nitrile and C16 acid, but the presence of Pt was required for hydrogenation and hydrogenolysis activity. The differences in the activity and selectivity of the catalysts could primarily be attributed to the properties of the support.

The Lewis acid properties of the supports influenced the selectivity towards the initial C16 amide conversion route and the activity for HDO of the oxygen-containing intermediate products. Accordingly, the catalysts were divided into four groups based on the strength of their Lewis acid sites, i.e., Si–Al ($Pt/\gamma-Al_2O_3$, $Pt/5SiO_2–95Al_2O_3$, $Pt/30SiO_2–$

This journal is © The Royal Society of Chemistry 2024

Catal. Sci. Technol., 2024, 14, 431–448 | 445

70Al$_2$O$_3$), Ti–Nb (Pt/TiO$_2$, Pt/Nb$_2$O$_5$), Ce–Zr (Pt/ZrO$_2$, Pt/CeO$_2$–ZrO$_2$), and Si (Pt/SiO$_2$). The intermediate strength Lewis acid sites of the Ti–Nb group were decisive for the activity and selectivity towards the dehydration of C16 amide to C16 nitrile, distinguishing the reaction network of the Ti–Nb group from the other groups. The Si–Al and Ce–Zr groups initially produced oxygen-containing and nitrogen-containing intermediate products with a similar selectivity, but the oxygen-containing intermediate products were converted more efficiently on the Ce–Zr group. The HDO activity of the Ce–Zr group could be related to their oxophilic weak Lewis acid sites.[29,85–90] The activity of the Si group was inferior to the other groups due to a lack of Lewis acid sites, which were required for several reactions. The preferred condensation reaction pathway and the yields of the C32 condensation products were influenced by the initial C16 amide conversion route and HDO activity and, consequently, differed between the catalyst groups.

The differences in the HDN activity of the catalyst groups were more subtle than the differences in the HDO activity. With an increasing batch residence time, it nevertheless became evident that the high HDO activity of the Ce–Zr and Ti–Nb groups was also beneficial for HDN activity, as the inhibition of HDN by the presence of oxygen-containing compounds was suppressed, regardless of the favored oxygen removal pathway. The importance of the HDO activity could be observed from the inferior paraffin yield and accumulation of C32 condensation products on Pt/γ-Al$_2$O$_3$, compared with Pt/ZrO$_2$ and Pt/TiO$_2$ in the time-series experiments. Overall, the results of this study emphasize the influence of the Lewis acid properties of the catalyst support on the activity of noble metal catalysts for the HDO and HDN of compounds that are relevant for the production of renewable fuels.

Author contributions

Emma Verkama: conceptualization, investigation, methodology, formal analysis, visualization, writing – original draft, Sylvia Albersberger: conceptualization, writing – review & editing, project administration, Aitor Arandia: conceptualization, investigation, methodology, writing – review & editing, Kristoffer Meinander: investigation, formal analysis, writing – review & editing, Marja Tiitta: conceptualization, writing – review & editing, supervision, Reetta Karinen: conceptualization, writing – review & editing, supervision, Riikka L. Puurunen: conceptualization, writing – review & editing, supervision, project administration, funding acquisition.

Conflicts of interest

Non-disclosure agreement prevents researchers from disclosing conflict of interest.

References

1 A. S. Berenblyum, V. Ya. Danyushevsky, E. A. Katsman, T. A. Podoplelova and V. R. Flid, *Pet. Chem.*, 2010, **50**, 305.
2 H. Brännström, H. Kumar and R. Alén, *BioEnergy Res.*, 2018, **11**, 592.
3 T. Kandaramath Hari, Z. Yaakob and N. N. Binitha, *Renewable Sustainable Energy Rev.*, 2015, **42**, 1234.
4 K. Malins, *Fuel*, 2021, **285**, 119129.
5 P. M. Mortensen, J.-D. Grunwaldt, P. A. Jensen, K. G. Knudsen and A. D. Jensen, *Appl. Catal., A*, 2011, **407**, 1.
6 P. Šimáček, D. Kubička, G. Šebor and M. Pospíšil, *Fuel*, 2009, **88**, 456.
7 B. Veriansyah, J. Y. Han, S. K. Kim, S.-A. Hong, Y. J. Kim, J. S. Lim, Y.-W. Shu, S.-G. Oh and J. Kim, *Fuel*, 2012, **94**, 578.
8 X. Li, X. Luo, Y. Jin, J. Li, H. Zhang, A. Zhang and J. Xie, *Renewable Sustainable Energy Rev.*, 2018, **82**, 3762.
9 P. Biller and A. B. Ross, *Bioresour. Technol.*, 2011, **102**, 215.
10 T. Madl and M. Mittelbach, *Analyst*, 2005, **130**, 565.
11 E. Furimsky and F. E. Massoth, *Catal. Rev.: Sci. Eng.*, 2005, **47**, 297.
12 G. Meitzner, *J. Catal.*, 1986, **98**, 513.
13 M. Cattenot, E. Peeters, C. Geantet, E. Devers and J. L. Zotin, *Catal. Lett.*, 2005, **99**, 171.
14 S. Ding, C. M. A. Parlett and X. Fan, *Mol. Catal.*, 2021, 111492.
15 M. Snåre, I. Kubičková, P. Mäki-Arvela, K. Eränen and D. Yu. Murzin, *Ind. Eng. Chem. Res.*, 2006, **45**, 5708.
16 E. Verkama, P. Auvinen, S. Albersberger, M. Tiitta, R. Karinen and R. L. Puurunen, *Top. Catal.*, 2023, **66**, 1353.
17 O. Palardy, C. Behnke and L. M. L. Laurens, *Energy Fuels*, 2017, **31**, 8275.
18 K. Shimizu, W. Onodera, A. S. Touchy, S. M. A. H. Siddiki, T. Toyao and K. Kon, *ChemistrySelect*, 2016, **1**, 736.
19 R. Burch, C. Paun, X.-M. Cao, P. Crawford, P. Goodrich, C. Hardacre, P. Hu, L. McLaughlin, J. Sá and J. M. Thompson, *J. Catal.*, 2011, **283**, 89.
20 Y. Nakagawa, R. Tamura, M. Tamura and K. Tomishige, *Sci. Technol. Adv. Mater.*, 2015, **16**, 014901.

446 | *Catal. Sci. Technol.*, 2024, **14**, 431–448

This journal is © The Royal Society of Chemistry 2024

21 J. R. Cabrero-Antonino, R. Adam, V. Papa and M. Beller, *Nat. Commun.*, 2020, **11**, 3893.

22 T. Toyao, S. M. a. H. Siddiki, Y. Morita, T. Kamachi, A. S. Touchy, W. Onodera, K. Kon, S. Furukawa, H. Ariga, K. Asakura, K. Yoshizawa and K. Shimizu, *Chem. – Eur. J.*, 2017, **23**, 14848.

23 J. Coetzee, H. G. Manyar, C. Hardacre and D. J. Cole-Hamilton, *ChemCatChem*, 2013, **5**, 2843.

24 M. Stein and B. Breit, *Angew. Chem., Int. Ed.*, 2013, **52**, 2231.

25 A. M. Smith and R. Whyman, *Chem. Rev.*, 2014, **114**, 5477.

26 M. Liu, Y. Shi, K. Wu, J. Liang, Y. Wu, S. Huang and M. Yang, *Catal. Commun.*, 2019, **129**, 105726.

27 J. Liang, R. Ding, Y. Wu, Y. Chen, K. Wu, Y. Meng, M. Yang and Y. Wang, *J. Mol. Catal. A: Chem.*, 2016, **411**, 95.

28 Y. Zhang, L. Li, F. Liu, H. Qi, L. Zhang, W. Guan, Y. Liu, A. Wang and T. Zhang, *ACS Catal.*, 2022, **12**, 6302.

29 O. U. Valdés-Martínez, J. N. Díaz de León, C. E. Santolalla, A. Talavera-López, H. Avila-Paredes and J. A. de los Reyes, *Ind. Eng. Chem. Res.*, 2021, **60**, 18880.

30 E. Mäkelä, J. L. González Escobedo, J. Neuvonen, J. Lahtinen, M. Lindblad, U. Lassi, R. Karinen and R. L. Puurunen, *ChemCatChem*, 2020, **12**, 4090.

31 K. A. Rogers and Y. Zheng, *ChemSusChem*, 2016, **9**, 1750.

32 K. Kon, W. Onodera, S. Takakusagi and K. Shimizu, *Catal. Sci. Technol.*, 2014, **4**, 3705.

33 A. M. Robinson, J. E. Hensley and J. W. Medlin, *ACS Catal.*, 2016, **6**, 5026.

34 S. J. Tauster, *Acc. Chem. Res.*, 1987, **20**, 389.

35 S. J. Tauster, S. C. Fung, R. T. K. Baker and J. A. Horsley, *Science*, 1981, **211**, 1121.

36 G. L. Haller and D. E. Resasco, in *Advances in Catalysis*, ed. D. D. Eley, H. Pines and P. B. Weisz, Academic Press, 1989, vol. 36, p. 173.

37 C.-J. Pan, M.-C. Tsai, W.-N. Su, J. Rick, N. G. Akalework, A. K. Agegnehu, S.-Y. Cheng and B.-J. Hwang, *J. Taiwan Inst. Chem. Eng.*, 2017, **74**, 154.

38 S. Brunauer, P. H. Emmett and E. Teller, *J. Am. Chem. Soc.*, 1938, **60**, 309.

39 E. P. Barrett, L. G. Joyner and P. P. Halenda, *J. Am. Chem. Soc.*, 1951, **73**, 373.

40 E. Bêche, P. Charvin, D. Perarnau, S. Abanades and G. Flamant, *Surf. Interface Anal.*, 2008, **40**, 264.

41 C. A. Emeis, *J. Catal.*, 1993, **141**, 347.

42 J.-Y. de Saint Laumer, E. Cicchetti, P. Merle, J. Egger and A. Chaintreau, *Anal. Chem.*, 2010, **82**, 6457.

43 M. Thommes, K. Kaneko, A. V. Neimark, J. P. Olivier, F. Rodriguez-Reinoso, J. Rouquerol and K. S. W. Sing, *Pure Appl. Chem.*, 2015, **87**, 1051.

44 M. Behrens and R. Schlögl, in *Characterization of Solid Materials and Heterogeneous Catalysts*, 2012, p. 609.

45 L. Deng, H. Miura, T. Shishido, S. Hosokawa, K. Teramura and T. Tanaka, *Chem. Commun.*, 2017, **53**, 6937.

46 N. S. de Resende, J.-G. Eon and M. Schmal, *J. Catal.*, 1999, **183**, 6.

47 J. A. Wang, A. Cuan, J. Salmones, N. Nava, S. Castillo, M. Morán-Pineda and F. Rojas, *Appl. Surf. Sci.*, 2004, **230**, 94.

48 D. A. G. Aranda, A. L. D. Ramos, F. B. Passos and M. Schmal, *Catal. Today*, 1996, **28**, 119.

49 H. Lieske, G. Lietz, H. Spindler and J. Völter, *J. Catal.*, 1983, **81**, 8.

50 C. Bozo, N. Guilhaume, E. Garbowski and M. Primet, *Catal. Today*, 2000, **59**, 33.

51 A. Ruiz Puigdollers, P. Schlexer, S. Tosoni and G. Pacchioni, *ACS Catal.*, 2017, **7**, 6493.

52 C. Nico, T. Monteiro and M. P. F. Graça, *Prog. Mater. Sci.*, 2016, **80**, 1.

53 S. B. T. Tran, H. Choi, S. Oh and J. Y. Park, *J. Catal.*, 2019, **375**, 124.

54 D. L. Hoang and H. Lieske, *Catal. Lett.*, 1994, **27**, 33.

55 T. Huizinga, J. Van Grondelle and R. Prins, *Appl. Catal.*, 1984, **10**, 199.

56 G. Pacchioni, *Phys. Chem. Chem. Phys.*, 2013, **15**, 1737.

57 M. Yu. Smirnov and G. W. Graham, *Catal. Lett.*, 2001, **72**, 39.

58 S. Eriksson, S. Rojas, M. Boutonnet and J. L. G. Fierro, *Appl. Catal., A*, 2007, **326**, 8.

59 J. A. Wang, T. López, X. Bokhimi and O. Novaro, *J. Mol. Catal. A: Chem.*, 2005, **239**, 249.

60 S. Bernal, J. J. Calvino, G. A. Cifredo, A. Laachir, V. Perrichon and J. M. Herrmann, *Langmuir*, 1994, **10**, 717.

61 L. V. Mattos and F. B. Noronha, *J. Power Sources*, 2005, **145**, 10.

62 J. Kašpar, P. Fornasiero and M. Graziani, *Catal. Today*, 1999, **50**, 285.

63 C. Zhang, H. He and K. Tanaka, *Appl. Catal., B*, 2006, **65**, 37.

64 H. Hattori, *Chem. Rev.*, 1995, **95**, 537.

65 G. Busca, *Catal. Today*, 2020, **357**, 621.

66 G. Busca, *Phys. Chem. Chem. Phys.*, 1999, **1**, 723.

67 M. Tamura, K. Shimizu and A. Satsuma, *Appl. Catal., A*, 2012, **433–434**, 135.

68 M. I. Zaki, M. A. Hasan, F. A. Al-Sagheer and L. Pasupulety, *Colloids Surf., A*, 2001, **190**, 261.

69 R. C. R. Neto and M. Schmal, *Appl. Catal., A*, 2013, **450**, 131.

70 G. S. Foo, D. Wei, D. S. Sholl and C. Sievers, *ACS Catal.*, 2014, **4**, 3180.

71 D. Davidson and M. Karten, *J. Am. Chem. Soc.*, 1956, **78**, 1066.

72 D. T. Mowry, *Chem. Rev.*, 1948, **42**, 189.

73 M. Tamura, S. Ishikawa, M. Betchaku, Y. Nakagawa and K. Tomishige, *Chem. Commun.*, 2018, **54**, 7503.

74 R. Pestman, A. van Duijne, J. A. Z. Pieterse and V. Ponec, *J. Mol. Catal. A: Chem.*, 1995, **103**, 175.

75 R. Pestman, R. M. Koster, J. A. Z. Pieterse and V. Ponec, *J. Catal.*, 1997, **168**, 255.

76 R. Pestman, R. M. Koster, A. van Duijne, J. A. Z. Pieterse and V. Ponec, *J. Catal.*, 1997, **168**, 265.

77 N. Sivasankar and R. Prins, *J. Catal.*, 2006, **241**, 342.

78 C. Zhu, O. Y. Gutiérrez, D. M. Santosa, M. Flake, R. Weindl, I. Kutnyakov, H. Shi and H. Wang, *Appl. Catal., B*, 2022, **307**, 121197.

This journal is © The Royal Society of Chemistry 2024

Catal. Sci. Technol., 2024, **14**, 431–448 | **447**

79 M. H. Al-Huniti and M. P. Croatt, *Asian J. Org. Chem.*, 2019, **8**, 1791.

80 I. Sorribes, S. C. S. Lemos, S. Martín, A. Mayoral, R. C. Lima and J. Andrés, *Catal. Sci. Technol.*, 2019, **9**, 6965.

81 S. Roy, G. Mpourmpakis, D.-Y. Hong, D. G. Vlachos, A. Bhan and R. J. Gorte, *ACS Catal.*, 2012, **2**, 1846.

82 P. Kostestkyy, J. Yu, R. J. Gorte and G. Mpourmpakis, *Catal. Sci. Technol.*, 2014, **4**, 3861.

83 E. Iglesia, D. G. Barton, J. A. Biscardi, M. J. L. Gines and S. L. Soled, *Catal. Today*, 1997, **38**, 339.

84 E. Peeters, M. Cattenot, C. Geantet, M. Breysse and J. L. Zotin, *Catal. Today*, 2008, **133–135**, 299.

85 P. M. de Souza, R. C. Rabelo-Neto, L. E. P. Borges, G. Jacobs, B. H. Davis, U. M. Graham, D. E. Resasco and F. B. Noronha, *ACS Catal.*, 2015, **5**, 7385.

86 C. A. Teles, P. M. de Souza, A. H. Braga, R. C. Rabelo-Neto, A. Teran, G. Jacobs, D. E. Resasco and F. B. Noronha, *Appl. Catal., B*, 2019, **249**, 292.

87 K. A. Resende, C. A. Teles, G. Jacobs, B. H. Davis, D. C. Cronauer, A. Jeremy Kropf, C. L. Marshall, C. E. Hori and F. B. Noronha, *Appl. Catal., B*, 2018, **232**, 213.

88 M. J. Mendes, O. A. A. Santos, E. Jordão and A. M. Silva, *Appl. Catal., A*, 2001, **217**, 253.

89 K. Kreuzer and R. Kramer, *J. Catal.*, 1997, **167**, 391.

90 J. Ni, W. Leng, J. Mao, J. Wang, J. Lin, D. Jiang and X. Li, *Appl. Catal., B*, 2019, **253**, 170.

91 M. Tamura, D. Yonezawa, T. Oshino, Y. Nakagawa and K. Tomishige, *ACS Catal.*, 2017, **7**, 5103.

92 H. Idriss, K. S. Kim and M. A. Barteau, in *Studies in Surface Science and Catalysis*, ed. R. K. Grasselli and A. W. Sleight, Elsevier, 1991, vol. 67, p. 327.

93 S. Foraita, J. L. Fulton, Z. A. Chase, A. Vjunov, P. Xu, E. Baráth, D. M. Camaioni, C. Zhao and J. A. Lercher, *Chem. – Eur. J.*, 2015, **21**, 2423.

94 B. Peng, C. Zhao, S. Kasakov, S. Foraita and J. A. Lercher, *Chem. – Eur. J.*, 2013, **19**, 4732.

95 T. Yokoyama and N. Yamagata, *Appl. Catal., A*, 2001, **221**, 227.

96 H. Tsuji and H. Hattori, *ChemPhysChem*, 2004, **5**, 733.

97 K. Tanabe and T. Yamaguchi, *Catal. Today*, 1994, **20**, 185.

98 A. N. Kay Lup, F. Abnisa, W. M. A. W. Daud and M. K. Aroua, *Appl. Catal., A*, 2017, **541**, 87.

99 Y. Huang and W. M. H. Sachtler, *Appl. Catal., A*, 1999, **182**, 365.

100 J. Volf and J. Pašek, in *Studies in Surface Science and Catalysis*, ed. L. Cerveny, Elsevier, 1986, vol. 27, p. 105.

101 G. Meitzner, W. J. Mykytka and J. H. Sinfelt, *Catal. Lett.*, 1995, **32**, 335.

102 J. H. Sinfelt, *Catal. Lett.*, 1991, **9**, 159.

103 W. E. Farneth and R. J. Gorte, *Chem. Rev.*, 1995, **95**, 615.

104 M. Marafi and E. Furimsky, *Energy Fuels*, 2017, **31**, 5711.

105 H. Greenfield, *Ind. Eng. Chem. Prod. Res. Dev.*, 1967, **6**, 142.

106 A. J. Adamczyk, *Surf. Sci.*, 2019, **682**, 84.

107 Y. Huang and W. M. H. Sachtler, *Appl. Catal., A*, 1999, **182**, 365.

108 A. Baiker and W. Richarz, *Ind. Eng. Chem. Prod. Res. Dev.*, 1977, **16**, 261.

109 A. Baiker, W. Caprez and W. L. Holstein, *Ind. Eng. Chem. Prod. Res. Dev.*, 1983, **22**, 217.

110 S. Zhang, Z. Xia, Y. Zou, M. Zhang and Y. Qu, *Nat. Commun.*, 2021, **12**, 3382.

448 | *Catal. Sci. Technol.*, 2024, **14**, 431–448

This journal is © The Royal Society of Chemistry 2024